Ahlers *et al. Geothermal Energy* (2022) 10:10
https://doi.org/10.1186/s40517-022-00222-6

Geothermal Energy

REVIEW Open Access

The crustal stress field of Germany: a refined prediction

Steffen Ahlers[1*], Luisa Röckel[2], Tobias Hergert[1], Karsten Reiter[1], Oliver Heidbach[3,4], Andreas Henk[1], Birgit Müller[2], Sophia Morawietz[3,4], Magdalena Scheck-Wenderoth[5,6] and Denis Anikiev[5]

*Correspondence:
ahlers@geo.tu-darmstadt.de
[1] Engineering Geology, Institute of Applied Geosciences, TU Darmstadt, 64287 Darmstadt, Germany
[2] Technical Petrophysics, Institute of Applied Geosciences, KIT, 76131 Karlsruhe, Germany
[3] Seismic Hazard and Risk Dynamics, GFZ German Research Centre for Geosciences, 14473 Potsdam, Germany
[4] Institute for Applied Geosciences, TU Berlin, 10587 Berlin, Germany
[5] Basin Modelling, GFZ German Research Centre for Geosciences, 14473 Potsdam, Germany
[6] Department of Geology, Geochemistry of Petroleum and Coal, Faculty of Georesources and Material Engineering, RWTH Aachen University, Aachen, Germany
Full list of author information is available at the end of the article

Abstract

Information about the absolute stress state in the upper crust plays a crucial role in the planning and execution of, e.g., directional drilling, stimulation and exploitation of geothermal and hydrocarbon reservoirs. Since many of these applications are related to sediments, we present a refined geomechanical–numerical model for Germany with focus on sedimentary basins, able to predict the complete 3D stress tensor. The lateral resolution of the model is 2.5 km, the vertical resolution about 250 m. Our model contains 22 units with focus on the sedimentary layers parameterized with individual rock properties. The model results show an overall good fit with magnitude data of the minimum (S_{hmin}) and maximum horizontal stress (S_{Hmax}) that are used for the model calibration. The mean of the absolute stress differences between these calibration data and the model results is 4.6 MPa for S_{hmin} and 6.4 MPa for S_{Hmax}. In addition, our predicted stress field shows good agreement to several supplementary in-situ data from the North German Basin, the Upper Rhine Graben and the Molasse Basin.

Keywords: 3D geomechanical–numerical model, Stress tensor, Stress magnitudes, Stress state, Upper Rhine Graben, North German Basin, Molasse Basin, Germany

Introduction

The prediction of the recent crustal stress field is important for many applications regarding the exploitation or use of the subsurface, particularly for directional drilling, stimulation and exploitation of geothermal or hydrocarbon reservoirs. Another currently important application is the search for and long-term safety assessment of a high-level nuclear waste deposit. However, up to now the knowledge of the crustal stress field for Germany is limited. It is essentially based on two major databases regarding stress tensor orientations and stress magnitudes (Heidbach et al. 2016; Morawietz et al. 2020), several 2D numerical models (Grünthal and Stromeyer 1994; Marotta et al. 2002; Kaiser et al. 2005; Jarosiński et al. 2006; Cacace et al. 2008) and some regional scale 3D geomechanical–numerical models (Buchmann and Connolly 2007; Heidbach et al. 2014; Hergert et al. 2015; Ziegler et al. 2016). The only large scale 3D model that covers entire Germany has been presented by Ahlers et al. (2021a). However, this model focuses on the large-scale stress pattern in the entire crust with low resolution in sediments that are represented with homogeneous mean rock properties.

To take a further step towards a robust prediction of the recent crustal stress state, we developed a geomechanical–numerical model of Germany based on Ahlers et al. (2021a). It provides a continuous prediction of the crustal stress in 3D with focus on the sedimentary basins. The work of Ahlers et al. (2021a) also provided a continuous description of the stress state of Germany but focused on basement structures and included a homogenous sedimentary layer without mechanical stratification in a coarse resolution. The model presented here has been significantly improved with a differentiated sedimentary layer, consisting of 15 units with specific material properties (density, Poisson's ratio and Young's modulus) and an 18-time higher resolution in the upper part of the crust. An improved differentiation of the sedimentary layer is essential, since the majority of applications focuses on sedimentary basins particularly for geothermal and hydrocarbon exploitation. At the same time, stress conditions within sedimentary units can be particularly challenging due to structural, lithological and mechanical variability. Mechanical properties varying with depth—mainly stiffness contrasts—can lead to differing stress magnitudes, differential stresses and perturbations in the orientation of the maximum horizontal stress (S_{Hmax}) (Cornet and Röckel 2012; Heidbach et al. 2014; Hergert et al. 2015). Extreme cases include very weak layers of salt or clay, leading to a nearly lithostatic stress state, which can mechanical decouple the overburden from the underburden layers (Roth and Fleckenstein 2001; Röckel and Lempp 2003; Heidbach et al. 2007; Ahlers et al. 2019). Furthermore, our new model is calibrated with minimum horizontal stress (S_{hmin}) and S_{Hmax} magnitudes which significantly improve the reliability of the predicted stress state compared to the model Ahlers et al. (2021a), which could only be calibrated with S_{hmin} values.

Model setup

Method

We assume linear elasticity and use the finite element method to solve the partial differential equations of the equilibrium of forces. First, an appropriate initial stress state is defined representing an undisturbed state of stress governed by gravity. In a second step, the stress state in the model is calibrated with magnitude data by varying displacement boundary conditions defined at the model edges. This modeling approach has been used for different tectonic settings and scales and is described in detail in Buchmann and Connolly (2007), Hergert and Heidbach (2011), Heidbach et al. (2014), Reiter and Heidbach (2014), Hergert et al. (2015) and Ahlers et al. (2021a). For the construction and discretization of the 3D model geometry and the assignment of rock properties to individual finite elements the software packages GOCAD™, HyperMesh™ and ApplePY (Ziegler et al. 2019) are used. As solver, we use the commercial finite element software package Abaqus™ v2019. For post-processing Tecplot 360™ enhanced with the GeoStress add-on (Stromeyer and Heidbach 2017) is used.

Geology of the study area

The diverse history of the model area lead to the complex geological structure observed today (Fig. 1c, d). The upper crust can be subdivided into four parts: the East European Craton (EEC) in the northeast amalgamated with Avalonia further south during the Caledonian orogeny, the Armorican Terrane Assemblage (ATA) added

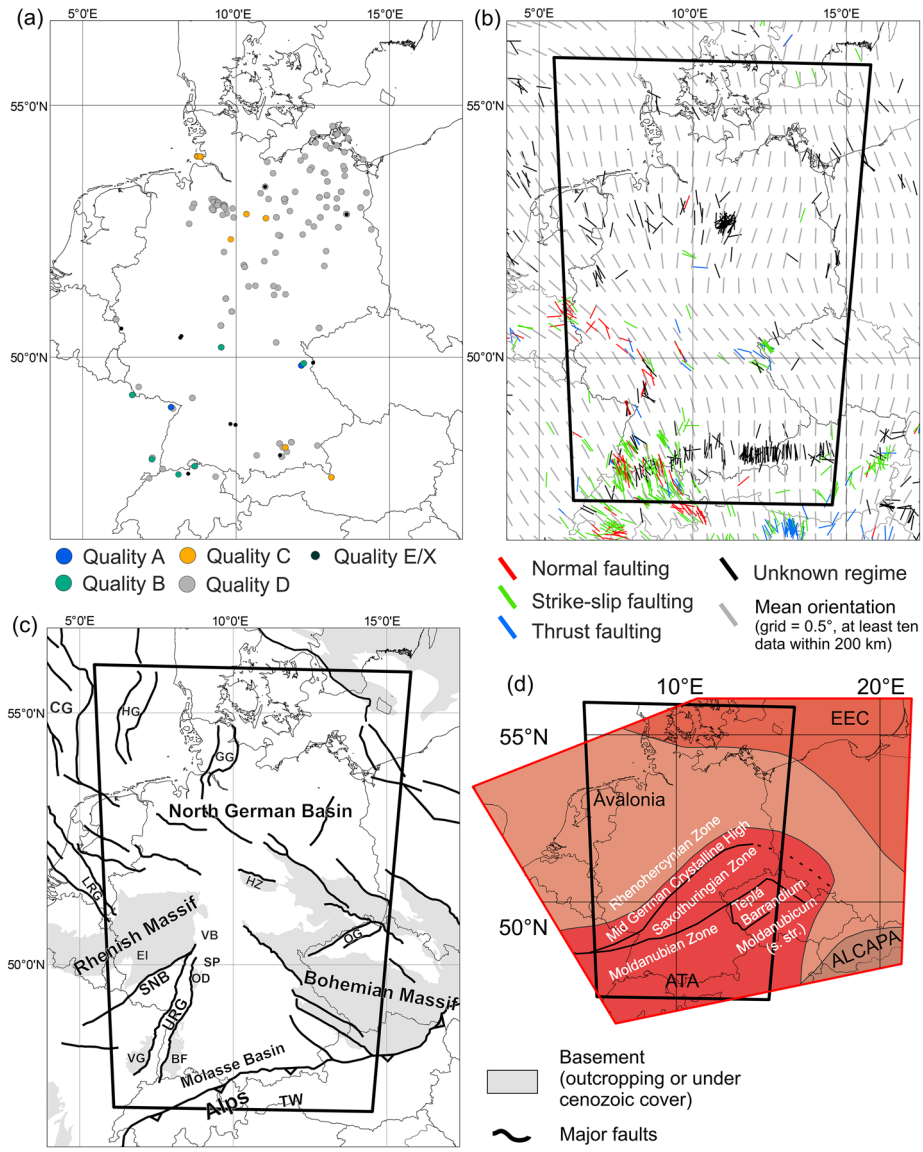

Fig. 1 Overview of the geology of the model region and stress data used for comparison and calibration. The black frame shows the key area of the model with increased stratigraphic resolution based on Anikiev et al. (2019). **a** Distribution of the stress magnitude data of Morawietz and Reiter (2020). The color-coded dots indicate the quality assigned by Morawietz et al. (2020). Displayed are all data from a true vertical depth (TVD) > 200 m. **b** Data of the World Stress Map (WSM) of Heidbach et al. (2016) and Levi et al. (2019). Color-coded lines indicate the stress regime and the orientation of S_{Hmax}. Grey lines show the mean orientation of S_{Hmax} on a regular grid (Details see chapter 3.1). **c** Geological framework of the model area based on Asch (2005) and Kley and Voigt (2008). BF—Black Forest, CG—Central Graben, EI—Eifel, HG—Horn Graben, HZ—Harz Mountains, GG—Glückstadt Graben, LRG—Lower Rhine Graben, OD—Odenwald, OG—Ohře Graben, SNB—Saar–Nahe Basin, SP—Spessart, TW—Tauern Window, URG—Upper Rhine Graben, VB—Vogelsberg Complex, VG—Vosges. **d** Overview of the basement structures based on Kroner et al. (2010) and Brückl et al. (2010). The red frame shows the entire model area. ALCAPA—Alps–Carpathian–Pannonian, ATA—Armorican Terrane Assemblage, EEC—East European Craton

during the Variscan orogeny and finally the Alp–Carpathian–Pannonian (ALCAPA) part as a result of the Alpine orogeny (Ziegler and Dèzes 2006; McCann 2008; Linnemann and Romer 2010). Since these units are identical to Ahlers et al. (2021a) we

refer to this publication for further information. The basement of the model area is mainly covered by late Paleozoic to Cenozoic sediments, with the exception of the Rhenish and Bohemian massifs commonly interpreted as long-lived highs (e.g., Eynatten et al. 2021), the Alpine mountain chain and parts of the Mid German Crystalline High (MGCH) and Moldanubian Zone (MDZ). During the final phase of the Variscan orogeny from the late Carboniferous to Permian time the model area was affected by extension leading to the origin of several basins filled up with debris of the eroding Variscan orogeny and contemporaneous volcanic activity mainly located in NE Germany (McCann et al. 2008; Scheck-Wenderoth et al. 2008). Due to the large amount of mostly reddish clastic and volcanic rocks deposited, this time period is called Rotliegend. The largest basin developed was the Southern Permian Basin with a maximum extent of ~ 1700 km covering large areas of the northern model area (Stollhofen et al. 2008). During the late Permian, this basin was flooded from the north leading to the deposition of the so-called 'Zechstein' evaporites (McCann et al. 2008). The following Triassic development of the model area was controlled by the breakup of Pangea and the westward opening of the Tethys leading to an E–W dominated extensional tectonic regime and the development of N–S-oriented graben systems mainly in the north, e.g., the Central Graben or the Glückstadt Graben (Fig. 1c) (Scheck-Wenderoth and Lamarche 2005; Kley et al. 2008). During this time period the southern 'Alpine' part of the model area was characterized by open marine conditions of the Tethys shelf, whereas continental to shallow marine conditions by repeated incursions of the Tethys dominated the northern 'Germanic' domain (Feist-Burkhardt et al. 2008). The Jurassic was dominated by the progressive breakup of Pangea and mostly marine conditions (Pienkowski et al. 2008). Central Europe was still affected by extensional tectonics but the extension direction changed to NW–SE during the Late Jurassic (Kley et al. 2008). During the Early Cretaceous this development continued with depocenters in the northern part of the model area (Voigt et al. 2008). However, the deposition of sediments was restricted to these depocenters that evolved as en echelon subbasins along the southern margin of the Permian Basin in a transtensional regime (Scheck-Wenderoth et al. 2008).The largest part of the former Permian Basin area in the northern domain of the model area was uplifted during Late Jurassic to Early Cretaceous times. In the Late Cretaceous the tectonic setting and depositional conditions changed. Due to an eustatic sea-level rise large parts of Central Europe were flooded and predominantly carbonates and sandstones were deposited (Scheck-Wenderoth et al. 2008). The rotation of Iberia reversed the tectonic regime leading to the inversion of former depocenters, the formation of thrust faults and basement uplifts, e.g., the Harz mountains (Kley et al. 2008). Additional processes for the Late Cretaceous to Paleogene exhumation are still discussed (Eynatten et al. 2021). The Cenozoic development of the model area was mainly influenced by the collision of Africa and Eurasia leading to the rise of the Alpine mountain chains and the evolution of the Molasse Basin (MB). In addition, the Cenozoic Rift System developed, e.g., the Upper Rhine Graben (URG) and the Lower Rhine Graben (LRG) (Ziegler and Dèzes 2006) and the uplift of the Rhenish Massif began (Reicherter et al. 2008). Except the sedimentary basins of the MB, the URG, the LRG and the North German Basin (NGB) large parts of the model area were affected by erosion (Rasser et al. 2008). The Cenozoic

tectonics north of the Alps were accompanied by various volcanic activities, e.g., the Vogelsberg Complex, the Eifel, Ohře Graben or in the vicinity of the URG (Litt et al. 2008; Reicherter et al. 2008).

Model geometry

All basic information about the model area and geometry is described in Ahlers et al. (2021a). However, to refine the resolution w.r.t. to the former model we subdivide the sediment layer. The subdivision is based on the 3D-Deutschland (3DD) model of Anikiev et al. (2019) and is, therefore, only resolved in the key area of our model (Fig. 2). We did not extend the higher stratigraphic resolution to the whole model area, since the data availability is poor and our focus area is covered by the 3DD data. Thus, the sedimentary units outside of the 3DD area are combined to a single unit. Furthermore, the stress data used for calibration are mainly located within the 3DD model area. The geometry data include a gap between the base of the Rotliegend—the deepest layer almost completely contained in the 3DD model—and the surface of the crystalline basement of Ahlers et al. (2021a). All lithological units between are represented by one unit named Pre-Permian unit though we aware that this is a very heterogeneous unit comprising early- to mid-Paleozoic low-grade metamorphic sediments and late-Paleozoic sediments.

Model discretization

The average lateral resolution of the model is 2.5 km and constant over the entire depth range of the model, the vertical resolution varies with depth. The mesh is divided into three vertical zones with a decreasing resolution with increasing depth. The deepest and most coarsely resolved unit is the lithospheric mantle limited by the bottom of the model and the Mohorovičić discontinuity with five element layers leading to a vertical resolution of 10 to 15 km. The mesh of the crust is subdivided at 10 km depth. Below 10 km depth the mesh contains ten element layers with a vertical resolution between 2.5 and 4 km. Above 10 km depth the mesh contains 43 element layers with a vertical resolution of about 240 m. Overall, the mesh contains about 11.1 million hexahedral elements.

Due to the complex geometry of the individual layers, especially of the sedimentary units, we did not create an individual mesh for each of them. We use ApplePY (Ziegler et al. 2019) to assign the individual mechanical properties of each unit to the finite elements of the mesh. Therefore, apart from the lithospheric mantle, which is the deepest meshed zone, the geometry of the individual units are not directly represented by the mesh. The final model consists of 22 units (Table 1): the lithospheric mantle, the lower crust, four units of the upper crust (EEC, Avalonia, ATA, ALCAPA), the Pre-Permian unit, Rotliegend volcanics and sediments, Zechstein carbonates and salt, Mesozoic units of the Triassic, Jurassic and Cretaceous, thrusted units of the Alps, folded units of the MB, three lateral subdivided units of Cenozoic sediments (NGB, URG and MB), Cenozoic volcanics and the sediments outside the 3DD area. In addition, there are some relict elements (Table 1, Layer ID: 2) which arise from the element assignment with ApplePY if the surface of the mesh does not fit perfectly to the surface defined by the geometry used. This occurs, because the geometry of the 3DD model has a higher resolution (1×1 km) than the mesh of our model ($\sim 2.5 \times 2.5$ km).

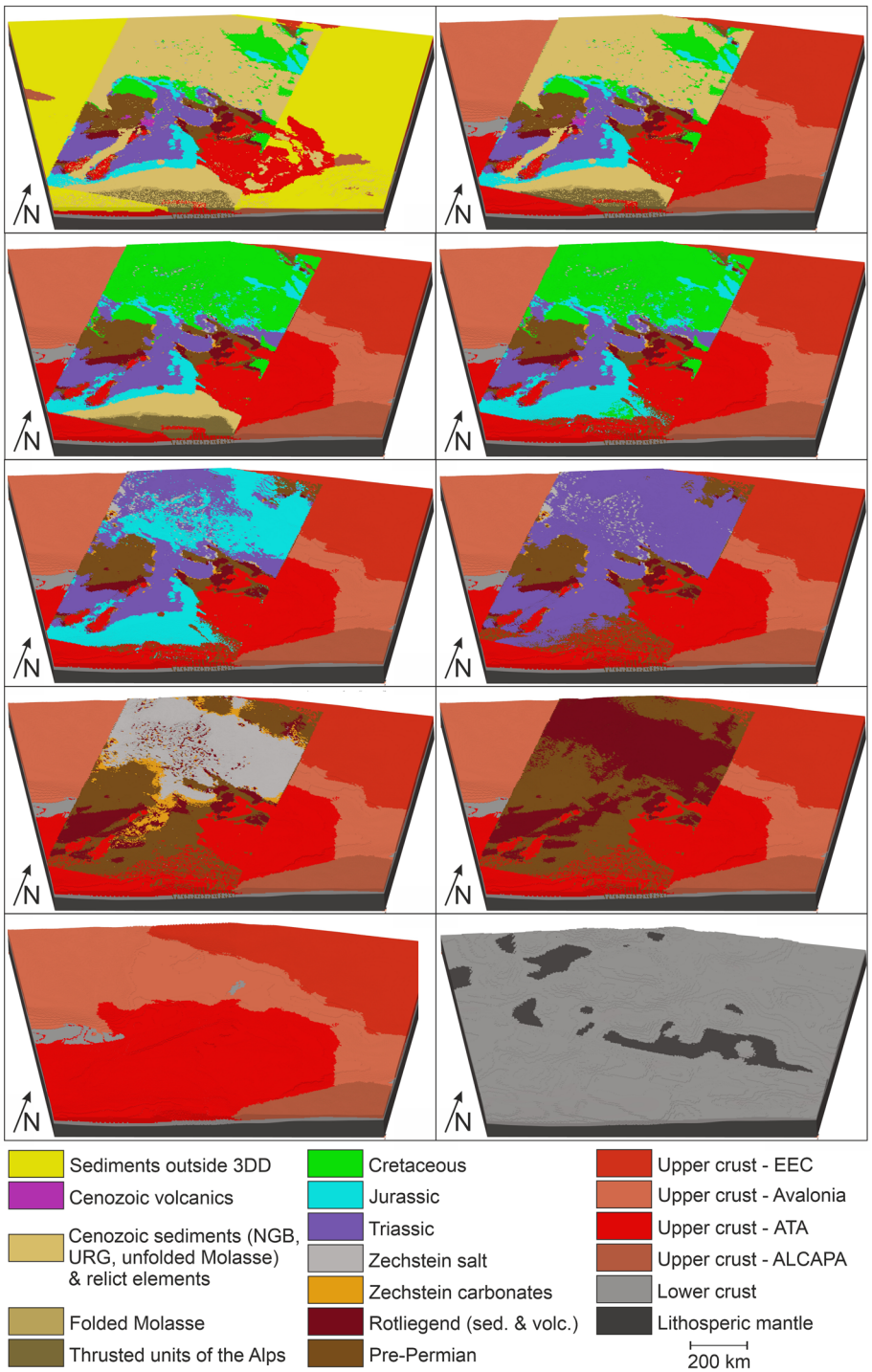

Fig. 2 Overview of the discretized model showing the internal structure including 22 units. ATA—Armorican Terrane Assemblage, ALCAPA—Alpine–Carpathian–Pannonian, EEC—East European Craton, NGB—North German Basin, URG—Upper Rhine Graben

Table 1 Overview of all units defined in the model and parameters used

Layer ID	Name	Density (kg/m^3)	Young's modulus (GPa)	Poisson's ration (−)	Friction angle (°)	Cohesion (MPa)	Tensile strength (MPa)
2	Relict elements	2400[a]	15[b]	0.29[b]	38[b]	10[b]	5
3	Sediments outside 3DD	2700	30	0.25	38[b]	10[b]	5
4	Cenozoic volcanics	2860[a]	54[c]	0.25[c]	50[i]	39[i]	5
5	Cenozoic sediments of the NGB	2480[a]	15[b]	0.29[b]	38[b]	10[b]	5
6	Cenozoic sediments of the URG	2300[a]	15[b]	0.29[b]	38[b]	10[b]	5
7	Cenozoic sediments of the Molasse Basin	2350[a]	15[b]	0.29[b]	38[b]	10[b]	5
8	Folded Molasse	2400[a]	15[b]	0.29[b]	38[b]	10[b]	5
9	Thrusted units of the Alps	2700[a]	23[c]	0.25[c]	40	25	5
10	Cretaceous	2590[a]	20[c]	0.25[c]	40[j]	18[j]	7[k]
11	Jurassic	2600[a]	20[c]	0.26[c]	36[b,j]	15[b,j]	5
12	Triassic	2650[a]	28[c]	0.25[c]	36[b,j]	31[b,j]	5
13	Zechstein salt	2100[a]	25[g]	0.27[g]	–	–	–
14	Zechstein carbonates	2400[a]	30[c]	0.25[c]	50[i]	18[i]	5
15	Rotliegend sediments	2600[a]	15[c]	0.19[c]	43[l,m]	25[l,m]	5[l,m]
16	Rotliegend volcanics	2650[a]	26[c]	0.25[c]	40[l]	57[l]	15[l]
17	Pre-Permian	2670[a]	40[c]	0.25[h]	40[l,n]	15[l,n]	5[l,n]
18	Upper crust ALCAPA	2750[d]	70[h]	0.25[h]	40[b,c]	30[b,c]	5
19	Upper crust ATA	2790[e]	70[h]	0.25[h]	40[b,c]	30[b,c]	5
20	Upper crust AV	2820[d]	70[h]	0.25[h]	40[b,c]	30[b,c]	5
21	Upper crust EEC	2810[d]	70[h]	0.25[h]	40[b,c]	30[b,c]	5
22	Lower crust	3000[d,e]	80[h]	0.25[h]	40[b,c]	30[b,c]	5
1	Lithospheric mantle	3300[e,f]	130	0.25[h]	40[b,c]	30[b,c]	5

For abbreviations, see Fig. 2. Further detailed information on the individual units can be found in Anikiev et al. (2019) and Ahlers et al. (2021a)

[a] Anikiev et al. (2019), [b]Hergert et al. (2015), [c]Bär et al. (2020), [d]Maystrenko and Scheck-Wenderoth (2013), [e]Tašárová et al. (2016), [f]Przybycin et al. (2015), [g]Wenting et al. (2017), [h]Turcotte and Schubert (2014), [i]Zoback (2007), [j]Reyer (2013), [k]Dubelaar and Nijland (2016), [l]Alber et al. (2015), [m]Stöckhert et al. (2013), [n]Alber and Solibida (2017)

Rock properties

Individual material properties are assigned to all 22 units of the model (Table 1). The density and the elastic properties (Young's modulus and Poisson's ratio) are defined as material properties for the numerical calculation, i.e., linear-elastic material behavior is assumed. Friction angle, cohesion and tensile strength are only used for post-processing analysis later on. Although our model contains 22 units, the Triassic and Jurassic units still contain mechanically very different subunits. For example, the Triassic unit comprises the sandstone-dominated Buntsandstein, the carbonate- and evaporate-dominated Muschelkalk and the claystone-dominated Keuper (Feist-Burkhardt et al. 2008).

Therefore, we calculated the arithmetic mean of the subunits for the mechanical properties of these two units. Another challenge was the parametrization of the thrusted units of the Alps, the sediments outside the 3DD area and the relict elements unit. Since the relict elements can only occur at the top of the model, we used an average value of the three Cenozoic sedimentary units (NGB, URG and MB). For the sediments outside of the 3DD model area, we have chosen roughly estimated values. For the thrusted units of the Alps, we decided to use the mean of the Mesozoic units with the exception of the density. As for almost all other units, we use the density values from the 3DD model of Anikiev et al. (2019). The elastic properties are mainly based on the P^3 database (Bär et al. 2020) and Hergert et al. (2015). In addition, the friction angle and cohesion are mainly based on the latter. The tensile strength is assumed to be 5 MPa for almost all units, since available data are limited. In general, all values in Table 1 without a reference are roughly estimated. The friction angle, cohesion and tensile strength of the Zechstein salt are not defined due to the visco-elastic properties of salt (e.g., Urai et al. 2008). In addition, we defined a Young's modulus gradient for all units with the exception of the sediments outside 3DD as it led to convergence problems at the model edges. The Young's modulus gradient should mimic the tendency of the rock mass to strengthen with increasing depth due to compaction and increasing confining pressure. An effect that can be seen, for example, in the decrease of porosity and permeability with increasing depth (Ingebritsen and Manning 1999). Our Young's modulus gradient reaches from 1.5 km depth to the surface, describing a reduction of the Young's modulus from 100% (of the values in Table 1) to 10% at the surface. The reduction to 10% is derived from Hudson and Harrison (1997) and the depth of the gradient was iterated by preliminary tests.

Initial stress state

An initial stress state is established, describing an only gravity-driven undisturbed, non-tectonic stress field within the upper crust before the displacement boundary conditions are applied. To achieve such an initial stress state, we extend our model with a sideburden (dark blue), an underburden (light blue) and a stiff shell (green) (Fig. 3a, b). The shell has a conic shape with a theoretical intersection point at the center of the earth emulating the naturally increasing confining pressure with depth (Zang and Stephansson, 2010). The elastic properties (Young's modulus and Poisson's ratio) of the sideburden and underburden are the adjusting screws to set a best-fit initial stress state. For calibration we use a semi-empirical function of Sheorey (1994) describing the undisturbed stress state of the earth as stress ratio (k):

$$k = \frac{S_{\mathrm{Hmean}}}{S_V} = \frac{S_{\mathrm{Hmax}} + S_{\mathrm{hmin}}}{2S_V} \tag{1}$$

depending on depth (z) and Young's modulus (E):

$$k = 0.25 + 7\mathrm{E}\left(0.001 + \frac{1}{z}\right) \tag{2}$$

we compare the theoretical k values with k values of our model using 29 virtual wells up to 25 km true vertical depth (TVD) (blue dots in Fig. 2a). Subsequently, we vary the

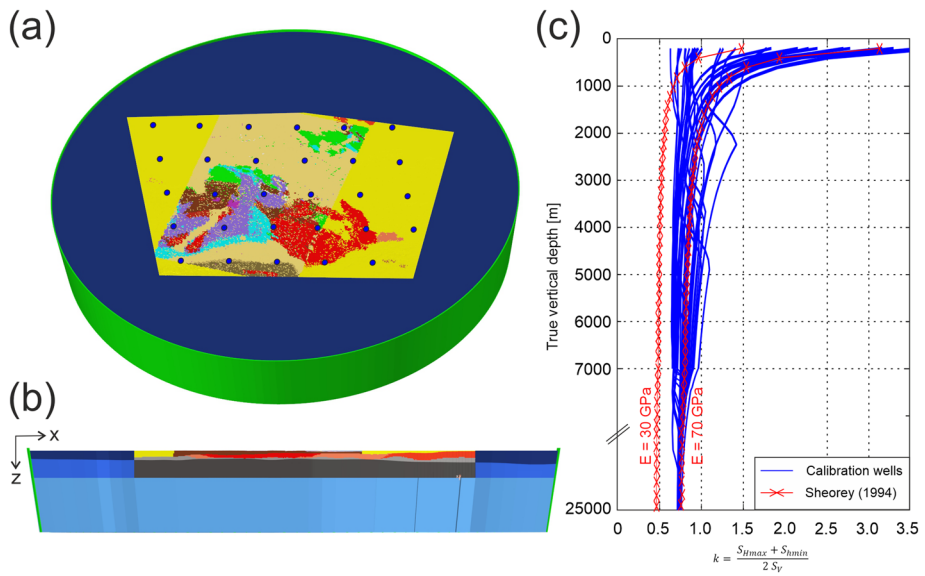

Fig. 3 Top (**a**) and side view (**b**) of the extended model box used to achieve an initial stress state. **c** Best-fit of 29 virtual wells (blue curves) and blue dots in **a** in comparison to calculated curves (red) for a Young's modulus of 30 and 70 GPa based on Sheorey (1994). There is a change of the scale of the depth axis below 7000 m TVD

gravity-driven settlement of the model by varying the Young's modulus of the underburden and increase or decrease the influence of S_V on the horizontal stresses by varying the Poisson's ratio within the model and the sideburden. This workflow has been used and described in detail by several authors before, e.g., Buchmann and Connolly (2007), Hergert (2009), Hergert and Heidbach (2011), Reiter and Heidbach (2014) or Ahlers et al. (2021a).

Our best-fit regarding the theoretical stress state of Sheorey (1994) is displayed in Fig. 3c. There is a change of scale along the depth axis below 7000 m TVD, since a uniform stress state and an almost perfect fit to the theoretical curve (red curve) is achieved at greater depths when all wells reach the upper crustal units (Layer ID: 18–21) with a homogeneous Young's modulus of 70 GPa. About half of the calibration wells (blue curves) show an almost vertical progression within the upper 1500 m, while the other half follows the progression of the theoretical curve of Sheorey (1994) to higher k values with decreasing depth. This effect occurs due to the Young's modulus gradient defined within the main area of our model up to 1500 m TVD. Figure 3c includes the function of Eq. (2) for a Young's modulus of 30 GPa typical for the sediments and a Young's modulus of 70 GPa representing crystalline basement units.

Displacement boundary conditions and calibration

After the initial stress state is reached, the model is calibrated with measured in-situ stress data using variable displacement boundary conditions. The bottom of the model is fixed vertically, horizontal displacements are allowed and the model surface is free. Displacement boundary conditions are defined at the five vertical model edges (Fig. 4). The directions of displacements are predefined by the mean S_{Hmax} orientation derived from the *World Stress Map* (WSM, Heidbach et al. 2016) data (Ahlers et al. 2021a). At

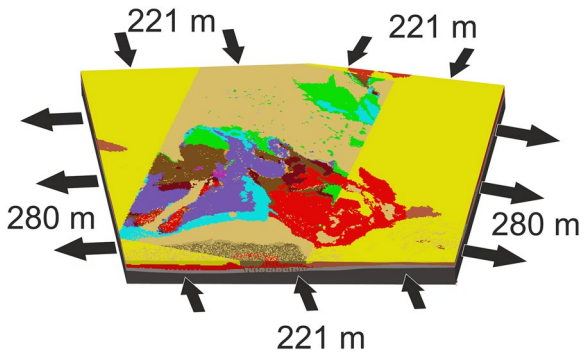

Fig. 4 Displacement boundary conditions applied at the discretized model. Arrows indicate direction of the displacements applied, numbers the magnitudes of displacements defined for the best-fit

the northern and southern edges, where S_{Hmax} is oriented perpendicular to the model boundary, compression is applied. Accordingly, extension is applied at the western and eastern edges, where S_{Hmax} is parallel to the model boundary. The magnitudes of the displacement boundary conditions are derived through a calibration process using in-situ stress magnitudes from the database of Morawietz and Reiter (2020). Since S_V is based almost entirely on density and is not influenced by displacement boundary conditions applied, only the S_{Hmax} and S_{hmin} magnitudes are used for calibration. We use only data qualities from A to C and values from TVDs > 200 m to minimize possible topographical effects. Thus, in total 73 S_{hmin} and 56 S_{Hmax} magnitudes from 200 to ~ 4700 m TVD are available from the database of Morawietz and Reiter (2020). Since the calibration data are unevenly distributed with depth (Figs. 6 and 8) a depth-weighted median for depth intervals of 500 m is used as decisive calibration value. The best-fit is achieved with a total shortening of 442 m in N–S direction and an extension of 560 m in E–W direction (Fig. 4).

Results

Orientation of S_{Hmax}

The orientations of S_{Hmax} in comparison to the mean orientation of S_{Hmax} derived from the WSM (Heidbach et al. 2016) and additional data by Levi et al. (2019) are displayed in Fig. 5. Figure 5a shows the modelled S_{Hmax} orientation at 5000 m TVD (red lines) and the mean S_{Hmax} orientation (black lines) with standard deviation (grey wedges) based on the WSM data. The angular deviation between these two are displayed as a color plot (Fig. 5b) and a histogram (Fig. 5c). The mean orientation of S_{Hmax} and standard deviation based on the WSM data is calculated using the stress2grid script of Ziegler and Heidbach (2019b) that uses the statistics for circular data (Mardia, 1972). Input data within a 200 km search radius are weighted by data quality and distance to a point of the 0.5° × 0.5° grid (Ziegler and Heidbach, 2019a). Furthermore, at least 10 data records—with a quality of A to C—within the search radius must be available to return a mean S_{Hmax} orientation. In addition, data from the NGB within or above the Zechstein salt are sorted out to avoid effects due to salt decoupling (e.g., Roth and Fleckenstein 2001; Röckel and Lempp 2003 and Heidbach et al. 2007, since visco-elastic properties are not included in our model.

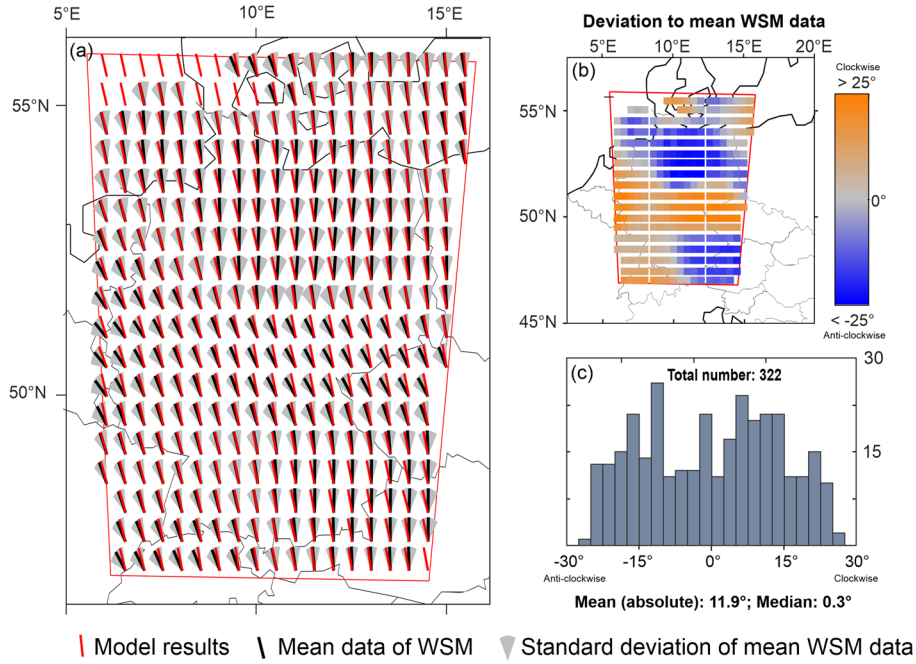

Fig. 5 Orientation of S_{Hmax} predicted by the model in comparison to the mean orientation of the WSM (Heidbach et al., 2016) and Levi et al. (2019). Details are described in the text. **a** Model results at 5 km TVD (red lines), the mean orientation derived from the WSM (black lines) with standard deviation (grey wedges). **b** Color-coded deviation between the results and the mean orientation of the WSM. Blue indicates an anti-clockwise rotation of the model results and orange a clockwise rotation of the model results w.r.t the mean orientation of the WSM. **c** Histogram showing the deviation displayed in **a** and **b**

As shown in Fig. 5a, our model predicts an almost homogeneous NNE–SSW orientated stress pattern. The median deviation of 0.3° indicates an overall good fit to the mean WSM data. Furthermore, almost all results are within the standard deviation of the mean WSM data. However, Fig. 5a, b indicates several model regions with significant deviations. For example, the local perturbations in the southern part of the model area where NW–SE orientations of S_{Hmax} dominate in the west and N–S orientations in the east or the NW–SE orientations in central Germany. In addition, the histogram (Fig. 5c) shows an uneven distribution of the deviation.

Stress magnitudes and absolute stress state

Magnitudes of S_{hmin}

The magnitudes of S_{hmin} predicted by the model are displayed in comparison to calibration data by Morawietz and Reiter (2020). The differences are calculated as model results minus calibration data. Thus, positive differences indicate too high values predicted by the model and negative differences too low values. The differences in Fig. 6a, c are color-coded regarding their qualities. We use 73 values, from TVDs > 200 m, with a quality of A to C from twelve localities mainly located in south Germany with the exception of a data record from Peckensen (Röckel and Lempp 2003). The localities are displayed in Fig. 6b with numbers indicating multiple magnitudes from different depths at one location. In general, the fit regarding the S_{hmin} magnitudes of Morawietz and Reiter (2020) is

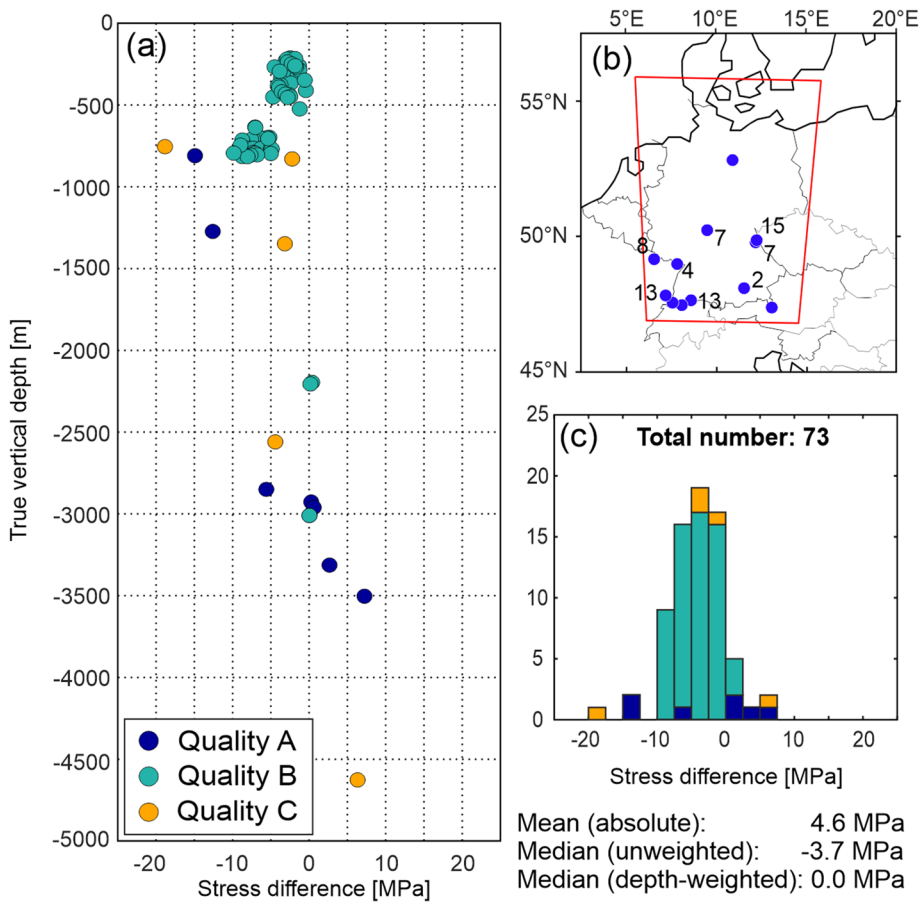

Fig. 6 S_{hmin} magnitudes of the model in comparison to data of Morawietz and Reiter (2020) used for calibration. **a** Color-coded differences versus depth. Differences are calculated as model results minus calibration data. **b** Spatial distribution of stress magnitude data, used for calibration. Numbers indicate localities with multiple data records. **c** Color-coded histogram of the differences displayed in **a**

good with differences in the range of −20 to 7.5 MPa and a mean of the absolute differences of 4.6 MPa. Figure 6a shows a depth trend from negative differences in the upper 1500 m indicating too low magnitudes predicted by the model to positive differences in greater depths indicating slightly too high magnitudes predicted. Due to the large amount of data in the upper 1000 m this leads to the unweighted median of −3.7 MPa and skewed histogram with a peak at −2.5 to −5 MPa. Therefore, we decided to use a depth-weighted median during the model calibration (chapter 2.7). A dependency on data qualities is not recognizable.

The depth sections displayed in Fig. 7 show the S_{hmin} magnitudes at 500, 1500, 2500 and 5000 m TVD. The S_{hmin} at 500 m TVD shows a homogeneous stress distribution with values mainly between 0 and 10 MPa. Only the northern and southern model edges show some larger magnitudes with the exception of the Tauern Window showing lower stresses equal to the main part of the model section. The section at 1500 m shows a less homogeneous stress distribution with dominant values between 10 and 30 MPa. The highest values, up to 70 MPa in the southeast, are again, related to the model boundaries. The lowest values (0 to 10 MPa) occur along the border between the Rhenoherzynian

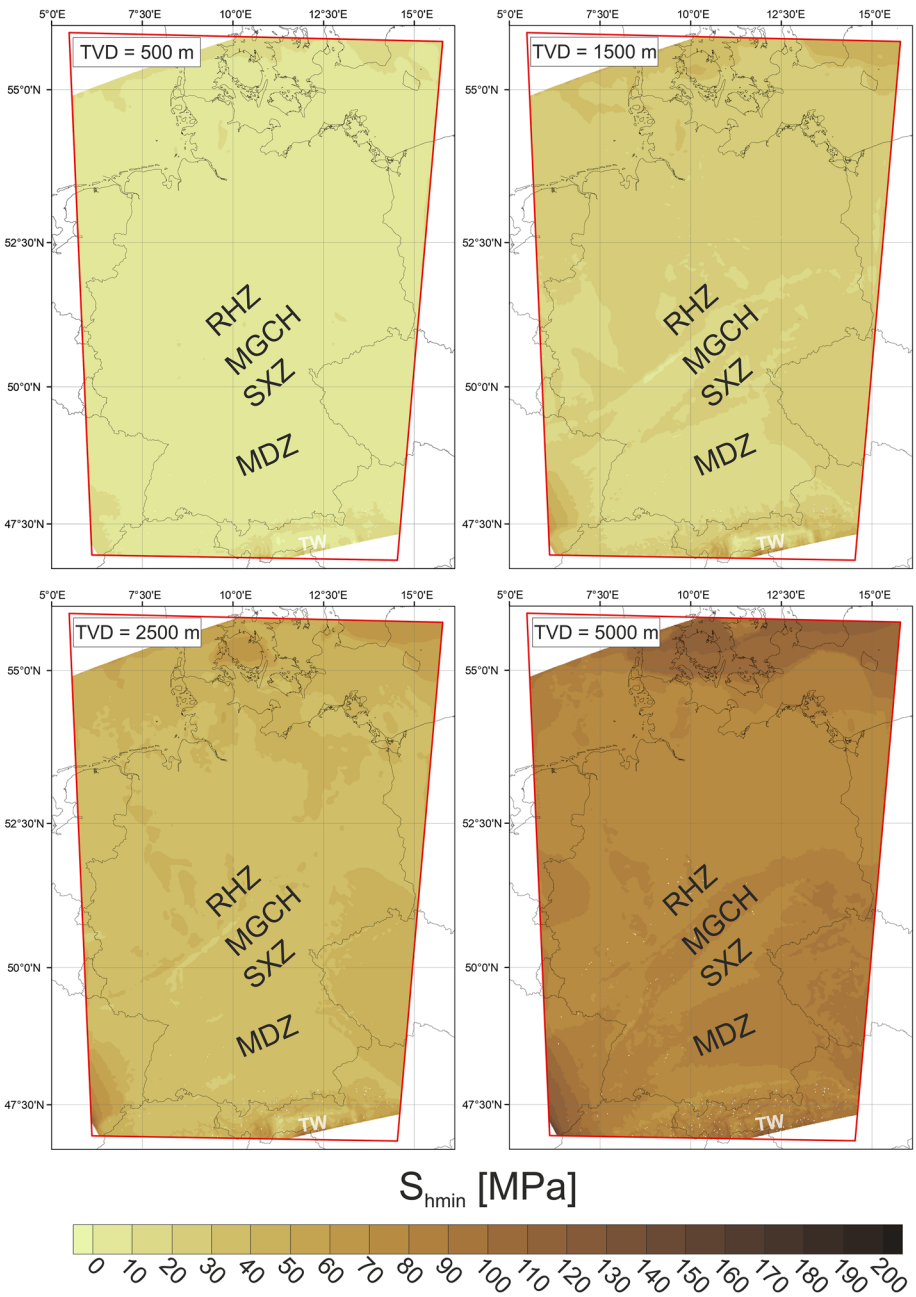

Fig. 7 Depth sections showing the lateral distribution of the S_{hmin} magnitudes predicted by the model at four depth sections. TVD—true vertical depth. Black titles (details in Fig. 1d): MDZ—Moldanubian Zone, MGCH—Mid German Crystalline High, RHZ—Rhenoherzynian Zone, SXZ—Saxothuringian Zone. White title (details in Fig. 1c): TW—Tauern Window

zone (RHZ) and the MGCH (Fig. 1d) and in the western part of the Tauern Window. Striking are the lower values (10 to 20 MPa) within the area of the MDZ and the MGCH. Sine, at 2500 m TVD these regions show the same magnitudes as the adjacent regions, in general, a homogeneous distribution with values between 30 and 40 MPa. The lowest values with 20 to 30 MPa again occur in the western part of the Tauern Window

and at the border between RHZ and MGCH. The highest values are associated with the model edges. At 5000 m TVD, the stress distribution within the area of the MDZ and the MGCH seems to be inverted in comparison to the distribution at 1500 m TVD, since the stress magnitudes are larger than in the adjacent areas, e.g., the Saxothuringian zone (SXZ). In general, the four depth sections of the model show a quite homogeneous distribution of S_{hmin} indicated by a maximum range of 20 to 30 MPa for each depth section, except for the model edges.

.

Magnitudes of S_{Hmax}

Figure 8 shows the S_{Hmax} magnitudes of the model in comparison to the calibration data of Morawietz and Reiter (2020). Differences displayed in Fig. 8a and c are calculated as model results minus calibration data. Thus, positive differences indicate too high values of S_{Hmax} predicted by the model and negative differences too low S_{Hmax} magnitudes predicted. The differences are color-coded depending on their qualities defined in the magnitude database by Morawietz et al. (2020). The localities of the data used are displayed

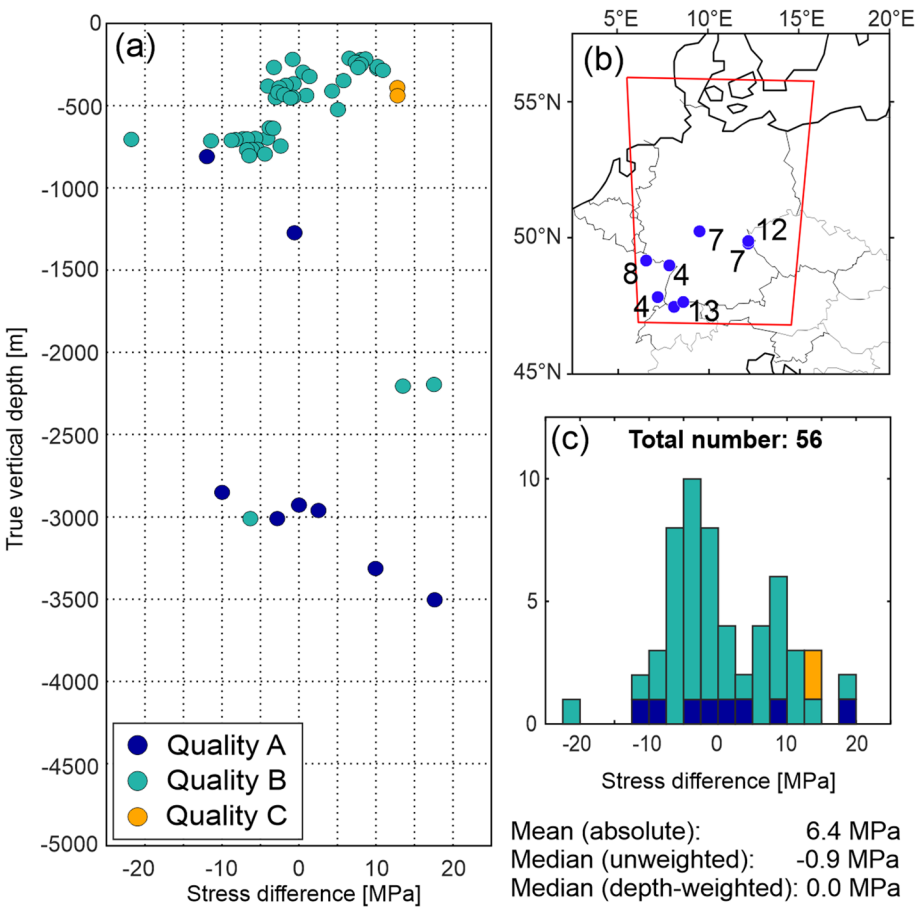

Fig. 8 S_{Hmax} magnitudes of the model in comparison to data of Morawietz and Reiter (2020) used for calibration. **a** Color-coded differences versus depth. Differences are calculated as model results minus calibration data. **b** Spatial distribution of stress magnitude data, used for calibration. Numbers indicate localities with multiple data records. **c** Color-coded histogram of the differences displayed in **a**

in Fig. 8b. All data used, with a quality of A to C and from a TVD > 200 m are located at eight localities in southern Germany. The differences versus depth (Fig. 8a) and the histogram (Fig. 8c) show a uniform distribution with a scattering of ± 20 MPa. A dependency of depth or quality is not visible. The homogeneous fit between the model results and the calibration data is also indicated by the (unweighted) median of − 0.9 MPa, which is almost equal to the depth-weighted median of 0.0 MPa. However, we also use the weighted median for the calibration with the S_{Hmax} magnitudes as for the S_{hmin} magnitudes to use a constant calibration value.

To show the lateral distribution of the S_{Hmax} magnitudes four horizontal sections at 500, 1500, 2500 and 5000 m TVD are displayed in Fig. 9. At 500 m TVD, the magnitudes range from 0 to 30 MPa. The lowest magnitudes with 0 to 10 MPa are located within the MGCH in the vicinity to the RHZ and in the Tauern Window. The highest values of > 20 MPa are associated with the model edges in the north and south and the basement outcrops of the southwestern Rhenish Massif, the Bohemian Massif, the Vosges, the Black Forest, the Odenwald and the Spessart. The section at 1500 m TVD shows a more differentiated distribution of S_{Hmax} with values ranging from 20 to 60 MPa, with some exception along the model edges. The higher values are again associated with outcropping basement structures, such as the Bohemian Massif. Regions with lower S_{Hmax} magnitudes between 20 and 40 MPa are located in the MB, the URG, the Saar–Nahe Basin (SNB), the NGB and the northern part of the MGCH in the vicinity of the RHZ. The results at 2500 and 5000 m TVD confirm the trend of higher magnitudes within the areas belonging to basement structures and lower magnitudes belonging to sedimentary units. An exception is the southwestern part of the Rhenish Massif, where the magnitudes do not increase as much as within the areas of crystalline basements. Finally, at 5000 m TVD the higher S_{Hmax} magnitudes correspond to areas with outcropping or shallow lying crystalline basement structures and lower S_{Hmax} magnitudes to sedimentary or low-grade metamorphic units.

Magnitudes of S_V

The differences between S_V magnitudes and the data by Morawietz and Reiter (2020) are displayed in Fig. 10. They are calculated as model results minus data of the magnitude database. Thus, too high model results lead to positive differences, too low model results to negative differences. Since the S_V magnitudes depend almost entirely on the density and are not influenced by displacement boundary conditions applied, we did not use these data for calibration but for validation to check if the densities chosen are reasonable. We use 71 values of Morawietz and Reiter (2020) from twelve localities (Fig. 10b). As the results show, the data used from the 3DD model (Anikiev et al. 2019) are very appropriate. With the exception of two values at 750 and 3700 m TVD all differences are in the range of − 2.5 to 2.5 MPa, resulting in a mean of the absolute differences of 1.1 MPa and a median of 0.0 MPa.

Regime Stress Ratio

To indicate the stress regime predicted by the model, the Regime Stress Ratio (RSR) for four model sections at 500, 1500, 2500 and 5000 m TVD is shown in Fig. 11. The RSR is a unitless value between 0 and 3 describing seven stress states defined by

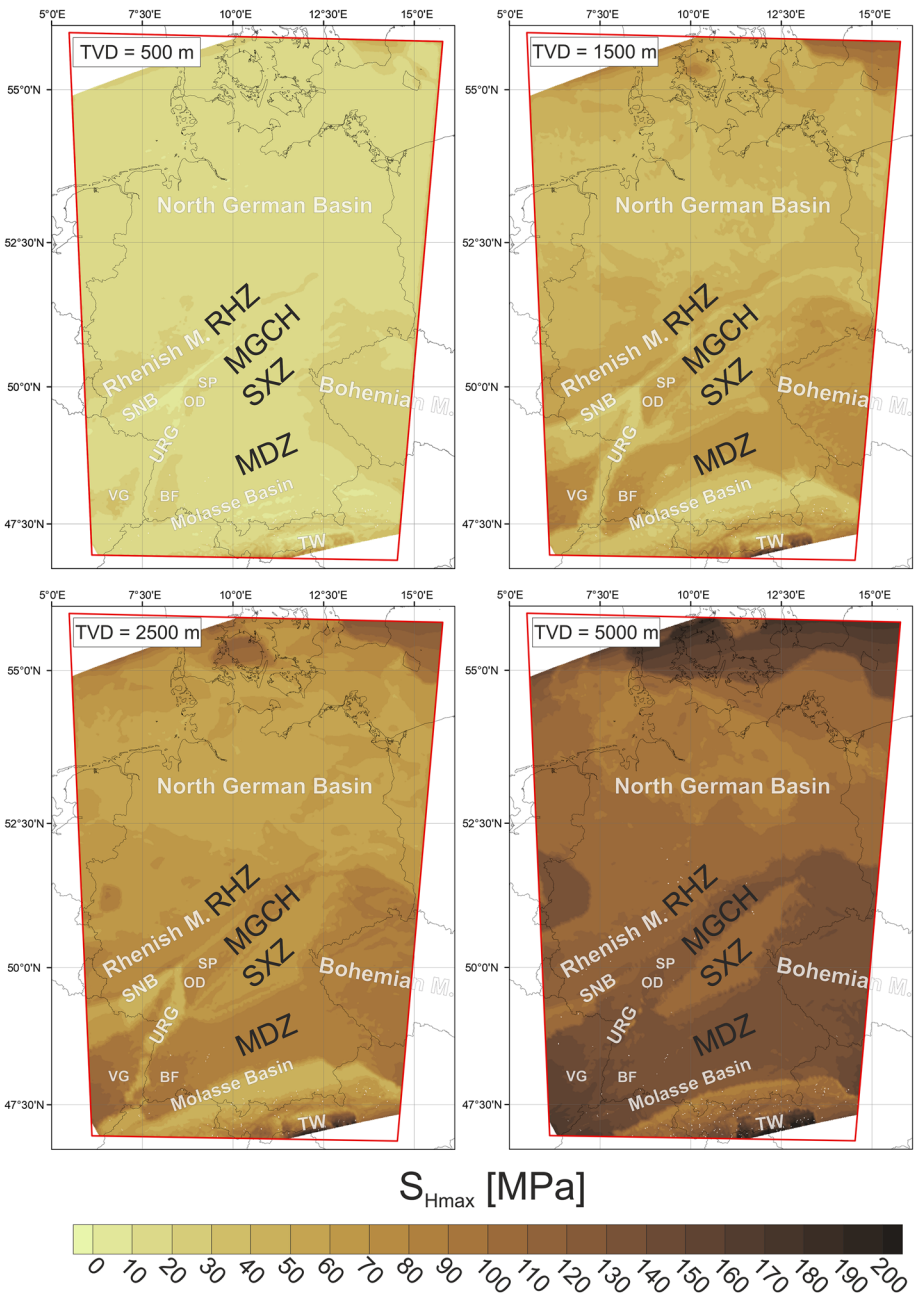

Fig. 9 Depth sections showing the lateral distribution of the S_{Hmax} magnitudes predicted by the model at four depth sections. TVD—true vertical depth. Black titles (details in Fig. 1d): MDZ—Moldanubian Zone, MGCH—Mid German Crystalline High, RHZ—Rhenoherzynian Zone, SXZ—Saxothuringian Zone. White titles (details in Fig. 1c): BF—Black Forest, M—Massif, OD—Odenwald, SNB—Saar–Nahe Basin, SP—Spessart, TW—Tauern Window, URG—Upper Rhine Graben, VG—Vosges

Simpson (1997): radial extension (0), pure normal faulting (0.5), transtension (1), pure strike-slip (1.5), transpression (2), pure reverse faulting (2.5) and constriction (3). The RSR (Eq. 3) is derived from the regime index n (Eq. 4, Anderson 1905) and the ratio of stress differences ϕ (Eq. 5, Angelier 1979):

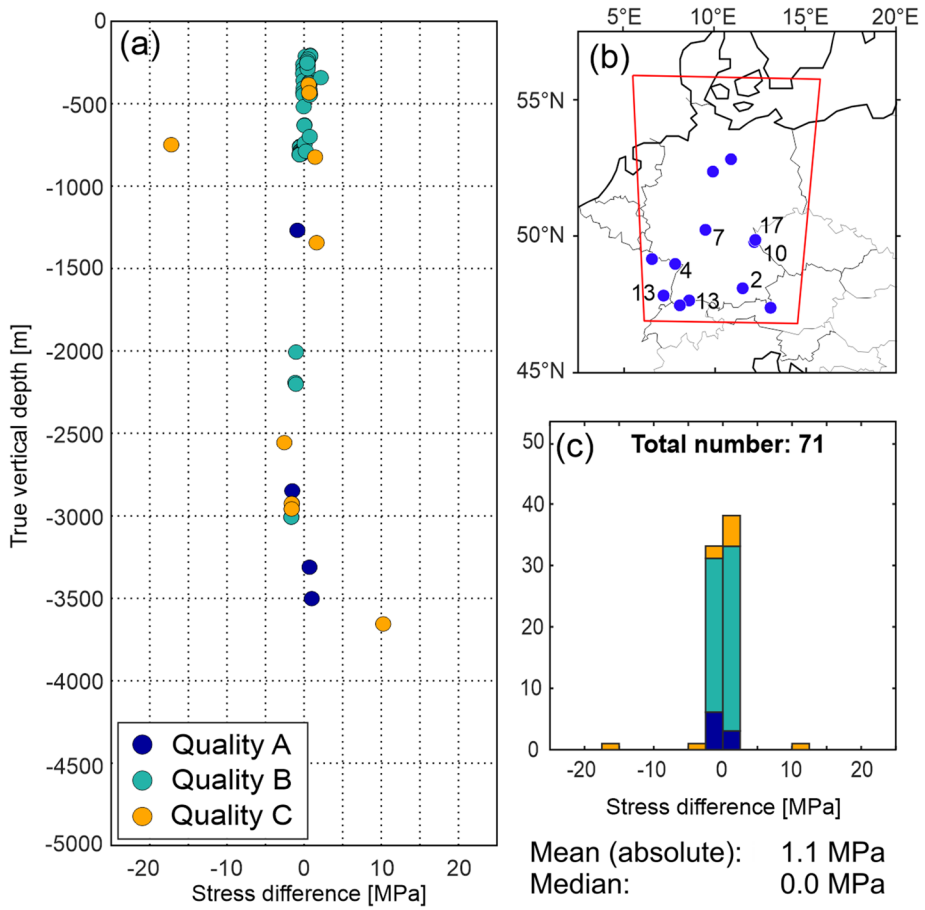

Fig. 10 S_V magnitudes of the model in comparison to data of Morawietz and Reiter (2020). **a** Color-coded differences versus depth. Differences are calculated as model results minus data of Morawietz and Reiter (2020). **b** Spatial distribution of stress magnitude data, used for comparison. Numbers indicate localities with multiple data. **c** Color-coded histogram of the differences displayed in **a**

$$\mathrm{RSR} = (n + 0.5) + (-1)^n(\phi - 0.5) \tag{3}$$

$$n = \begin{cases} 0 S_{\mathrm{hmin}} < S_{\mathrm{Hmax}} < S_V \\ 1 S_{\mathrm{hmin}} < S_V < S_{\mathrm{Hmax}} \\ 2 S_V < S_{\mathrm{hmin}} < S_{\mathrm{Hmax}} \end{cases} \tag{4}$$

$$\phi = \frac{(\sigma_2 - \sigma_3)}{(\sigma_1 - \sigma_3)} \tag{5}$$

The calculated RSR values at 500 m TVD show a very inhomogeneous distribution, displaying the whole range from thrust to normal faulting. Very high values—indicating a thrust faulting regime—can be found, e.g., at the model edges. Low values, indicating a normal faulting regime, occur, e.g., in the SNB, the URG, the NGB and in the MB. The model section at 1500 m TVD shows a more homogeneous pattern than at 500 m TVD. RSR values larger than 2 occur still at the model edges and within the area of the Glückstadt Graben. The lowest values still occur in the SNB, the URG, the NGB and some

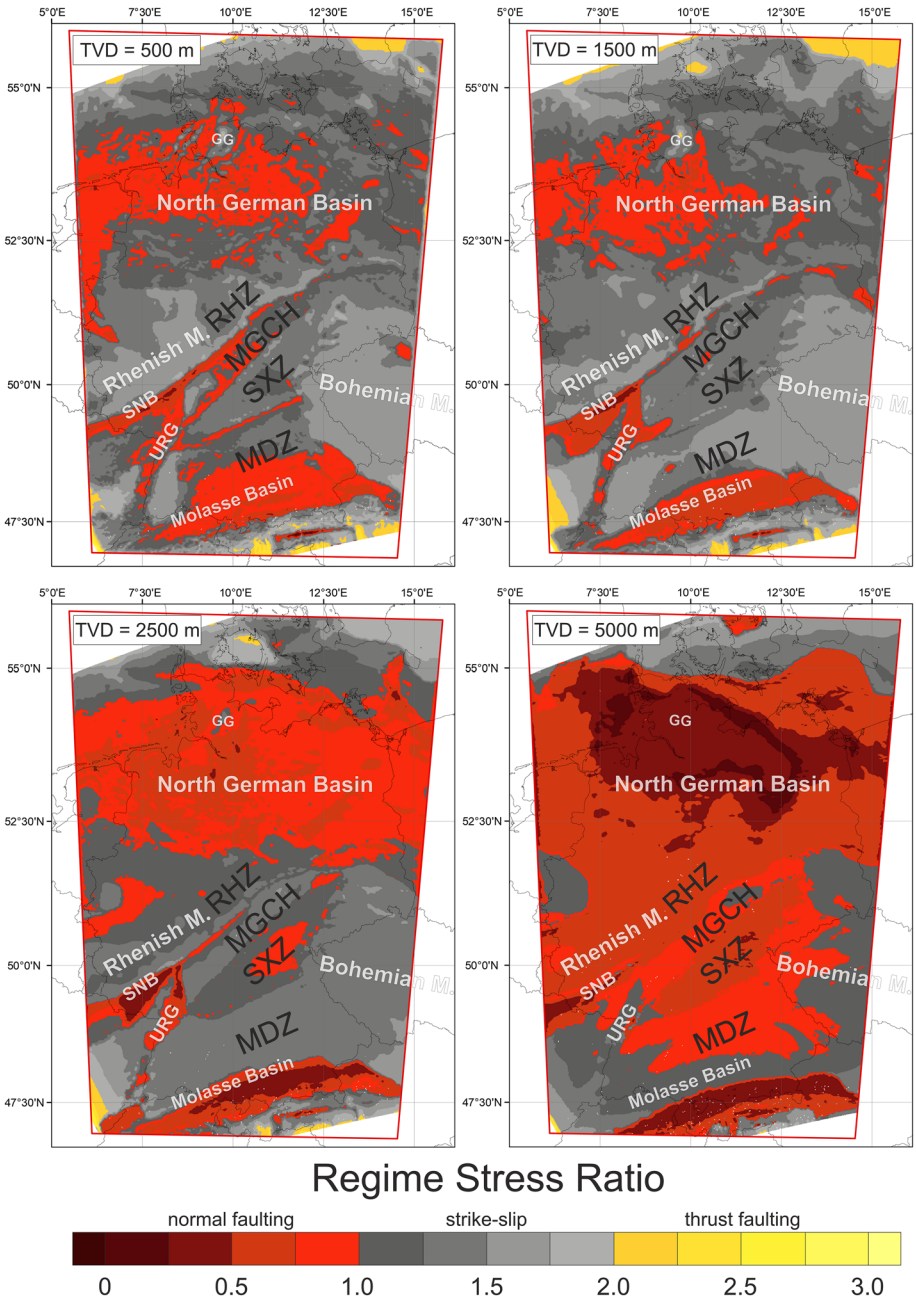

Fig. 11 Four depth sections showing the lateral distribution of the Regime Stress Ratio (RSR) predicted by the model. TVD—true vertical depth. Black titles (details in Fig. 1d): MDZ—Moldanubian Zone, MGCH—Mid German Crystalline High, RHZ—Rhenoherzynian Zone, SXZ—Saxothuringian Zone. White titles (details in Fig. 1c): GG—Glückstadt Graben, M—Massif, SNB—Saar–Nahe Basin, URG—Upper Rhine Graben

areas within the MB. This trend continues at 2500 m TVD. Here, almost the entire SNB show values < 0.5 indicating a pure normal faulting regime. As at 1500 m TVD, also the NGB and the southern part of the MB show a normal faulting regime and additionally also the SXZ. In contrast to the 1500 m TVD section, several regions show lower values at 2500 m TVD. The deepest model section shown at 5000 m TVD shows a much more

homogeneous distribution than at 500 m with large areas indicating a normal faulting regime. The trends described for 2500 m TVD continues, except within the URG. Up to a TVD of 2500 m the RSR in this area is lower in comparison to the surrounding areas, but at 5000 m TVD the RSR is higher.

Stress gradients

Figure 12 shows modeling results from three major sedimentary basins in Germany, the NGB, the URG and the MB, in comparison to available data partially also used for calibration. Results and data of the upper 200 m TVD are not displayed to avoid showing data influenced by topography or free surface effects. The model results are displayed as magnitude sets (S_V, S_{hmin} and S_{Hmax}) from virtual wells up to 8 km TVD located at the locations from which measurement data are shown. This results in a compilation of 12 magnitude sets for the MB, five magnitude sets for the URG and 45 magnitude sets for the NGB.

The results for the NGB show quite uniform magnitudes for all 45 magnitude sets displayed. The modeled S_{hmin} magnitudes show the smallest range of values with a maximum range of ~ 10 MPa except for two outliers below ~ 5000 m TVD. The range of the S_{Hmax} magnitudes are larger with an average range of ~ 15 MPa, a maximum of ~ 25 MPa at ~ 5000 m TVD and again two outliers. The S_V magnitudes show a trend of increasing scattering with depth, starting with a range of < 5 MPa at 200 m TVD to a range of ~ 20 MPa at 8 km TVD.

The five data sets from the URG show similar gradients for S_{hmin} and S_V but significant differences for the S_{Hmax} magnitudes. The S_{Hmax} magnitudes are also the only ones

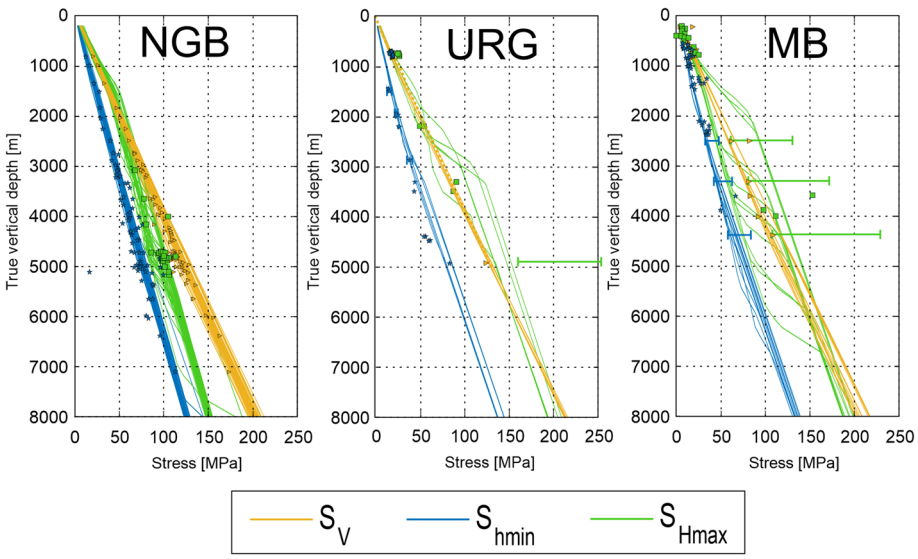

Fig. 12 Results from multiple virtual wells in the corresponding sedimentary basin of the model in comparison to measured and calculated magnitudes of S_V, S_{hmin}, and S_{Hmax}. The uncertainties of the magnitudes if specified are displayed as error bars. North German Basin (NGB): Röckel and Lempp (2003), Fleckenstein et al. (2004), Stöckhert et al. (2013). Upper Rhine Graben (URG): Cornet and Burlet (1992), Klee and Rummel (1993), Valley and Evans (2007), Häring et al. (2008), Meixner et al. (2014), Azzola et al. (2019). Molasse Basin (MB): nagra (2001), Seithel et al. (2015), Backers et al. (2017), Budach et al. (2017), Drews et al. (2019), Garrard et al. (2021)

that show significant changes of the gradients with depth. While the S_{hmin} and S_V magnitudes show an almost linear increase with depth, some S_{Hmax} magnitudes between 2000 and 3500 m increase sharply and some even show decreasing or constant values. The compilation of the MB shows the most inhomogeneous results. At about 1000 m TVD, the magnitudes of S_{Hmax} split in two groups. The magnitudes of three virtual wells show an increase to ~ 40 MPa at 2500 m TVD in contrast to nine virtual wells, which show continuous S_{Hmax} magnitudes. The S_V and S_{hmin} values of these three virtual wells also increase but less obviously to 5 to 10 MPa higher values. With increasing depth at about 2500, 3200, 3700, 4200, 5000 and 6000 m TVD, other virtual wells also show such increasing magnitudes and converge to the higher magnitude trend. In general, there seems to be a lower and a higher magnitude gradient with a transition zone between 1000 and 6500 m TVD changing from one dominating gradient (0–1000 m TVD) to another (> 6500 m TVD). At 8 km TVD, all magnitudes are roughly homogenous with S_{hmin} magnitudes of 130 to 140 MPa, S_{Hmax} magnitudes of 180 to 200 MPa and S_V magnitudes of 200 to 215 MPa.

Fracture Potential

As an additional result the Fracture Potential (FP) of four depth sections is displayed in Fig. 13. The FP based on Connolly and Cosgrove (1999) and Eckert and Connolly (2004) is a dimensionless value indicating how close to failure the stress state is. The calculation is described in detail by Heidbach et al. (2020). The FP is defined as actual maximum shear stress divided by the acceptable shear stress (Eq. 6):

$$\mathrm{FP} = \frac{actual\ maximum\ shear\ stress}{acceptable\ shear\ stress} \tag{6}$$

Therefore, an FP of > 1 indicates failure and lower FPs represent a stable state of stress. The *actual maximum shear stress* is calculated as mean of the maximum (σ_1) and minimum (σ_3) principal stress (Eq. 7):

$$actual\ maximum\ shear\ stress = \frac{1}{2}(\sigma_1 - \sigma_3) \tag{7}$$

The acceptable maximum shear stress is calculated as (Eq. 8):

$$acceptable\ shear\ stress = Ccos\phi + \frac{1}{2}(\sigma_1 + \sigma_3)sin\phi \tag{8}$$

The FP is calculated with individual cohesion (C) and friction angle (ϕ) for each model unit (Table 1), except for the Zechstein salt unit, since salt behaves visco-elastic. Therefore, the regions where Zechstein salt occur are left white in Fig. 13. The results in Fig. 13 show a stable stress state with an FP between 0 and 0.6. The highest values of 0.5 to 0.6 occur at 1500 m depth. In general, there is an increase of the FP up to 1500 m TVD. With further increasing depth the FP decreases. At 500 m TVD relative low values are associated with sedimentary units as within the NGB, the SNB or the Mesozoic units in southern Germany. Higher values are mainly associated with outcropping basement units, for example within the Bohemian and Rhenish Massif, the Vosges and the Black Forest. This trend is also visible at 1500 m TVD with

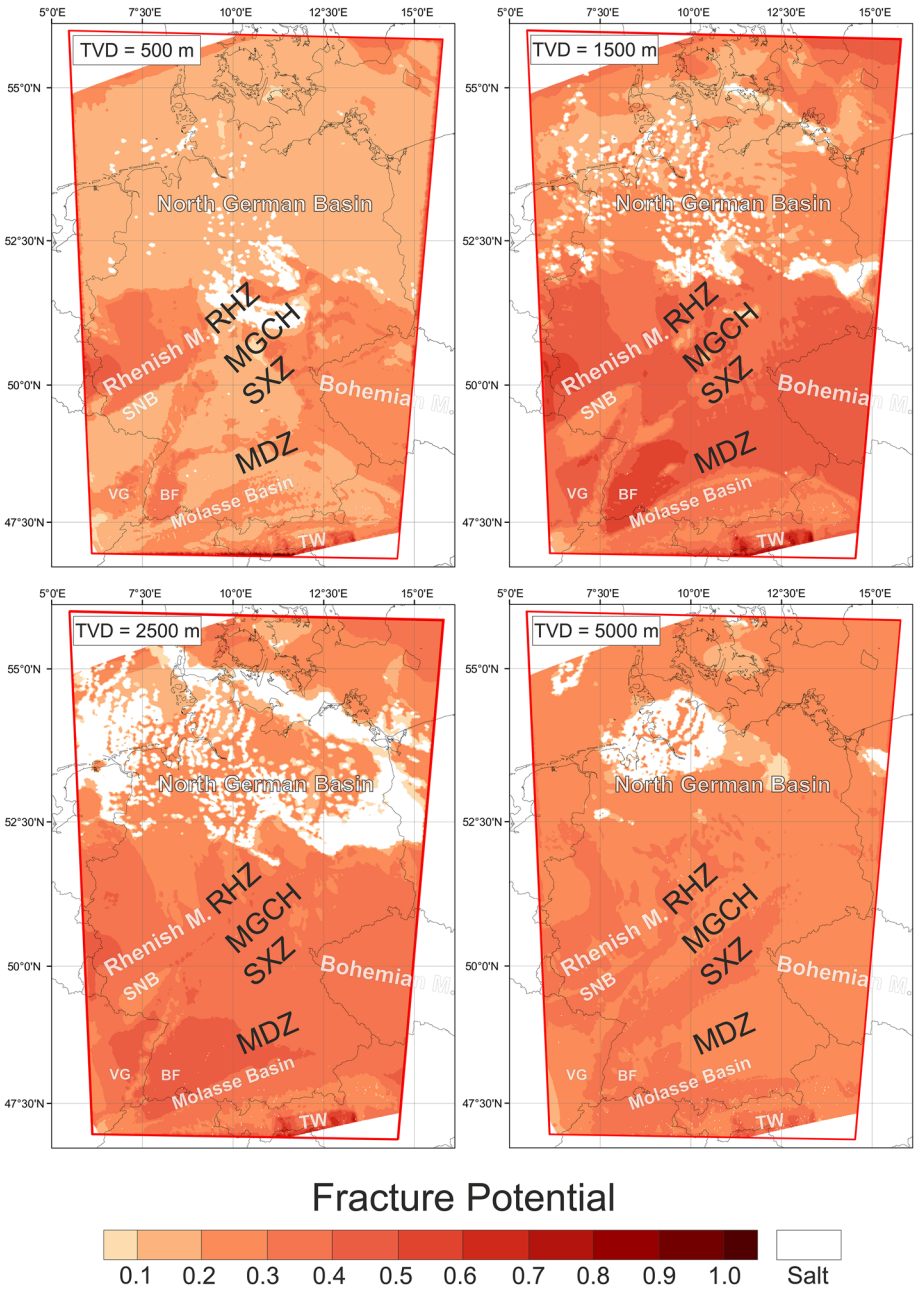

Fig. 13 Depth sections showing the lateral distribution of the Fracture Potential calculated for the model results. TVD—true vertical depth. Regions, where Zechstein salt occurs are left white. Black titles (details in Fig. 1d): MDZ—Moldanubian Zone, MGCH—Mid German Crystalline High, RHZ—Rhenoherzynian Zone, SXZ—Saxothuringian Zone. White titles (details in Fig. 1c): BF—Black Forest, M—Massif, SNB—Saar–Nahe Basin, TW—Tauern Window, VG—Vosges

a generally higher FP. High values are associated with crystalline basement units, e.g., the MDZ, the MGCH or the Tauern Window, low values are predicted for the NGB, the SNB or the MB. At 2500 m TVD such a clear trend is not visible anymore, but a low FP is still located within in the SNB. An interpretation of the results from the

NGB is difficult for this depth section, since the Zechstein salt unit is dominant here. At 5000 m TVD the NGB is still a region with a relative low FP. However, in contrast to the depth sections at 500 or 1500 m TVD some regions show opposite trends. For example, the Bohemian Massif with former relatively high values or the SNB with former relatively low values.

Discussion

Orientation of S_{Hmax}

Although our results lie almost entirely within the standard deviation of the S_{Hmax} orientation derived from the WSM and some additional data of Levi et al. (2019) and a median of deviation of 0.3° suggest a very good fit, a closer look indicates some discrepancies (Fig. 5). The orientations of S_{Hmax} predicted by our model (Fig. 5a) show a homogenous NNW–SSE pattern with some small deviation to N–S but the mean S_{Hmax} orientation of the WSM show several regions with divergent patterns, e.g., within the eastern part of the NGB showing N–S to NNE–SSW orientations or the central part of Germany with dominant NW–SE orientations. These results indicate that our model does probably not include some relevant factors or our displacement boundary conditions applied are too simple to reproduce the pattern of the orientation of S_{Hmax}. The median deviation of 0.3° and the distribution of the histogram support the former since differing displacements, e.g., at the eastern and western edges would probably only shift the distribution as a whole. Implemented lateral stiffness contrasts do not seem to have a significant impact on the regional stress field, e.g., predicted by Grünthal and Stromeyer (1994), Marotta et al. (2002) or Reiter (2021), despite Young's modulus contrasts of > 50 GPa, e.g., at the southern edge of the SNB between weak Rotliegend sediments (15 GPa) and the stiff upper crust (70 GPa). However, laterally there are no contrasts of the Young's modulus in the upper crystalline crust. Thus, the softer units lie on a homogeneous and stiff block. This could be an explanation of the quite homogeneous orientations of S_{Hmax} of our model within in the sedimentary units but also for parts of the crust, since our model assumption of linear elasticity does not represents the ductile behavior of lower parts of the crust and the mantle (e.g., Stüwe 2007).

Processes not included in our model, which may also affect the stress field within the model region, are isostatic buoyancy effects in Scandinavia (Kaiser et al. 2005) or in the south due to erosion, deglaciation and potential slab break off below the Alpine chain (Przybycin et al. 2015; Sternai et al. 2019). In addition, the lithosphere–asthenosphere-boundary (Cacace 2008) or density contrasts in the lower crust, e.g., the Pritzwalk anomaly (Krawczyk et al. 2008) could explain the misfit in the northeast. Effects due to salt decoupling leading to a regional stress field below and a more local stress field above the Zechstein unit (Roth and Fleckenstein 2001; Röckel and Lempp 2003; Heidbach et al. 2007) should have no influence, since we did not use the data from the units above.

Absolute stress and stress regime

In general, the predicted S_{hmin} magnitudes fit the values of Morawietz and Reiter (2020) quite well with differences between −20 and +7.5 MPa and a mean of the absolute differences of 4.6 MPa (Fig. 6) and an overall good fit to additional data in Fig. 12. However, the depth dependent differences (Fig. 6a) and the compilation

of the URG and the MB (Fig. 12) indicate too low magnitudes of S_{hmin} within the upper ~ 1500 m of the model. Since the shallow calibration data (Fig. 6b) and additional data of the MB (Fig. 12) are partly located in young sedimentary units, the Young's modulus in the model could possibly be too high for these units, despite the implemented Young's modulus gradient. Furthermore, unconsolidated sediments can behave in a visco-elastic manner (e.g., Chang and Zoback 1998; Zoback 2007), which the linear elastic properties of our model cannot represent. Both, a lower Young's modulus and visco-elastic properties would lead to higher S_{hmin} magnitudes, since the S_{hmin} magnitudes would approach the S_V magnitudes. Missing visco-elastic properties can also explain the too low values at ~ 800 m TVD, data from Wittelsheim, in the southwestern URG (Fig. 12) measured in an evaporitic layer (Cornet and Burlet 1992). Another clue to explain the low values could be the geographic distribution of the data. Almost all calibration data used and the data of the MB indicating this trend are located in the southern part of Germany. Available high quality data from the northern part of Germany are sparse, but the data used for comparison do not confirm this trend (Fig. 12). A possible trend to slightly too high values in the lower part of the model indicated by the three deepest values in the general comparison (Fig. 6) cannot be confirmed by the results in Fig. 12.

The predicted S_{Hmax} magnitudes also show a good fit to the values of the magnitude database by Morawietz and Reiter (2020) (Fig. 8) despite a wider range of differences between -20 and + 20 MPa and a higher mean of the absolute differences of 6.4 MPa in comparison to the S_{hmin} magnitudes. However, available S_{Hmax} magnitudes are usually calculated and not measured and, therefore, have larger uncertainties (Morawietz et al. 2020). Furthermore, calibration data from units which are parametrized with mean mechanical properties, e.g., the Triassic unit or from thin units which are numerically not sufficiently represented by our model resolution can explain the wider range. Since, differing stiffnesses have a significantly higher influence on S_{Hmax} magnitudes than on S_{hmin} magnitudes (Fig. 12). A quantification of the influence of mean properties on the results is possible, e.g., using the HIPSTER tool of Ziegler (2021) but not feasible for such a large-scale model, since thousands of calculations would be necessary for such an estimation.

Although the S_{Hmax} magnitudes of our model do not show a general depth trend as described for the S_{hmin} magnitudes, the differences in the upper 1000 m TVD show a distribution that is very similar to the one of the S_{hmin} magnitudes within this depth range (Figs. 6 and 8). This does not fit to the assumption that the Young's modulus might be too high, because too low S_{Hmax} values rather indicate too low Young's modulus values. Incorporation of visco-elastic properties could increase both magnitudes if the S_{Hmax} magnitudes are lower than S_V, which is partly the case indicated by a normal faulting regime in Figs. 11 and 12. Another possibility to increase both horizontal magnitudes at the same time is an increase of the vertical stress, a higher Poisson's ratio, a higher stress input due to the boundary conditions or a higher k ratio of the initial stress. Increasing stresses by increasing the density does not seem to make sense, since the fit with the S_V magnitudes (Fig. 10) is almost perfect. A higher Poisson's ratio for different units within this specific depth interval only is difficult to explain. The third and fourth possibility, an increased shortening and reduced

extension by the displacement boundary conditions or an increased k-ratio within the upper part of the model only, are difficult to implement and are difficult to explain from a tectonic point of view.

Another view inside the model is given by the compilation of virtual wells in Fig. 12. The magnitudes used for comparison from the NGB are mainly based on two data sets. A compilation of Röckel and Lempp (2003) from the eastern and central part of the NGB and a data set by Fleckenstein et al. (2004) from the western part of the NGB. The compilation of Röckel and Lempp (2003) only contains S_V and S_{hmin} magnitudes, the compilation of Fleckenstein et al. (2004) all three principal stresses. However, the data sets show some general differences. The data from Fleckenstein et al. (2004) show a near isotropic stress state, particularly well visible between 4750 and 5250 m where the stress magnitudes of S_{hmin}, S_{Hmax} and S_V are very close to each other. The smaller magnitudes of S_{hmin} and also the larger S_V magnitudes visible within this depth range are from Röckel and Lempp (2003). In general, the model results of all virtual wells displayed show a better fit to the data of Röckel and Lempp (2003). However, it is remarkable that the S_{Hmax} magnitudes contrary to the S_{hmin} and S_V magnitudes fit the data by Fleckenstein et al. (2004) quite well. The misfit between these data sets could be explained due to the different location within the NGB. Another possible reason for this discrepancy could be the different measurement methods, since the data by Fleckenstein et al. (2004) are based on core samples, while the data of Röckel and Lempp (2003) are in-situ measurements. However, despite these inconsistencies the overall fit of the model results to the displayed data within the NGB is good.

The fit of the second virtual well compilation for the URG in comparison to the predicted magnitudes is also good. Regarding the S_{hmin} magnitudes, the results show only significant differences to the measured magnitudes at 800 m TVD and between 3500 and 4500 m TVD. The differences at ~ 800 m TVD, indicating ~ 10 MPa too low magnitudes, are probably a result of inappropriate material properties in the model for this area. As mentioned before, these data set is measured in an evaporitic layer at Wittelsheim (Cornet and Burlet 1992). However, our model does not include visco-elastic properties. Between 3500 and 4500 m TVD the model results indicate a trend to too high S_{hmin}. However, the deepest data record at 5000 m TVD fits to the model results. The S_{Hmax} data in general show a wider range of values as the S_{hmin} data. At ~ 800 and ~ 5000 m TVD our results indicate too low values. However, the value at 5000 m TVD from Basel (Häring et al. 2008) must be interpreted with care due to the very high uncertainty indicated by the error bar. The differences between 2000 and 3500 m TVD show significant deviations up to ~ 30 MPa but all data records are within the range of our predicted values. At ~ 2200 m TVD the lowest differences occur for all locations, except the results from Soultz-sous-Forets. Although both measured S_{Hmax} magnitudes shown at 2200 m TVD are from Soultz-sous-Forets (Klee and Rummel 1993) the model results from this region indicate too high values.. A possible explanation are altered granites in the upper part of the crystalline basement as described by Aichholzer et al. (2016) which are not well represented by our high Young's modulus of 70 GPa. A lower Young's modulus would possibly lead to lower S_{Hmax} and a better fit. However, the altered granites are only about 150 m thick and, therefore, not able to explain the full discrepancy. Remarkable are the S_{Hmax} magnitudes between 2500 and 3500 m TVD predicted for Bruchsal,

showing a very low gradient leading to ~ 30 to 40 MPa lower values as predicted for the other locations. This trend can be explained by a thick Rotliegend layer within this region (GeORG-Projektteam 2013; Meixner et al., 2014), with a low Young's modulus of 15 GPa. In addition, four of the five virtual wells show a significant change of the S_{Hmax} gradients with depth. For example, Rittershoffen and Soultz-sous-Forets—located only ~ 10 km apart from each other—show almost similar S_{Hmax} values below 3000 m TVD, but the gradient change occur below 1500 m TVD at Soultz-sous-Forets and below 2250 m TVD at Rittershoffen. The depth at which the 'jump' of the S_{Hmax} magnitudes occurs fits quite perfectly to the boundary between the crystalline basement and the sedimentary units of the URG. Rittershoffen is a little east to Soultz-sous-Forets and further away from the western graben shoulder of the URG, and therefore, the top of the crystalline basement in Rittershoffen is located at ~ 2250 m TVD and at ~ 1550 m TVD in Soultz-sous-Forets (Aichholzer et al. 2016).

The S_{hmin} magnitudes of our model within the MB show a good fit to the comparison data displayed below 2000 m TVD. However, as already mentioned, our model results indicate partially too low values in the upper 1500 m. The S_{Hmax} magnitudes again show larger variations. Similar to the results of the URG, in all virtual wells the S_{Hmax} magnitudes increase if the crystalline basement is reached. Thus, since the depth of the crystalline basement differs in almost every virtual well due to the southward increase of the sediment thickness in the MB, the resulting stresses are inhomogeneous. A remarkable outlier is the data record at ~ 3600 m from Mauerstetten (Backers et al. 2017).

In general, the predicted S_{Hmax} magnitudes of the MB and URG show the impact of the vertical model resolution. The transition zone between sediments and crystalline basement is ~ 750 m, which corresponds to about three element rows. A higher model resolution could decrease this transition zone significantly.

Since the calibration data (Figs. 6 and 8) and the compilations of Fig. 12 only show pointwise data the S_{hmin} and S_{Hmax} magnitudes are additionally displayed by several depth sections to focus on the lateral distribution. In general, the depth sections of Fig. 7 displaying the lateral distribution of the S_{hmin} magnitudes show a more homogeneous pattern than the S_{Hmax} magnitudes in Fig. 9. However, in both figures high magnitudes of S_{hmin} or S_{Hmax} are associated with crystalline basement units, e.g., the Bohemian Massif in the southeast or the EEC in the northeast and low magnitudes are often related to sedimentary basins, e.g., the NGB or the MB or regions with outcropping low-grade metamorphic sediments, e.g., the RHZ or SXZ. This correlation can be explained by the combination of stiff units with relatively high densities and softer units, which often have lower densities. However, a high stiffness alone is not sufficient for high horizontal stress magnitudes. This is because high stiffness leads to an increase in S_{Hmax} magnitudes as a result of applied shortening but at the same time to a decrease in the S_{hmin} magnitude as a result of applied extension. Accordingly, a higher Young's modulus leads to higher S_{Hmax} magnitudes and lower S_{hmin} magnitudes. This effect can be reduced or increased by the influence of S_{V}. S_{V} reduces or increases the S_{hmin} and S_{Hmax} magnitudes equally, and since it is defined by density, a high density leads to higher horizontal stresses and a lower density to lower horizontal stresses. An example for this combined effect can be seen within the MDZ and MGCH, where an inversion of the S_{hmin} magnitudes relative to the adjacent regions

occurs between 1500 and 5000 m TVD (Fig. 7). The MDZ and MGCH are regions with a thin sedimentary cover. Therefore, the low S_{hmin} magnitudes at 1500 m occur due to the high Young's modulus of 70 GPa and a lower magnitude of S_V due to the thin sedimentary cover. The adjacent regions show higher S_{hmin} magnitudes, e.g., the Bohemian Massif with a similar Young's modulus but a higher S_V due to the missing sedimentary cover or the SXZ due to a lower Young's modulus and a higher S_V. At 5000 m TVD the MDZ and MGCH show higher S_{hmin} values than the SXZ but more similar to the ones in the Bohemian Massif. This shows that the effect of the thin sedimentary cover vanishes with depth. Furthermore, the relation between the S_{hmin} magnitudes in the Bohemian Massif and the RHZ and NGB shows that the influence of a higher density (Bohemian Massif > RHZ & NGB) exceeds the effect of a lower Young's modulus (RHZ & NGB < Bohemian Massif). The lateral distribution of the S_{Hmax} magnitudes is easier to explain, since a higher density and a higher Young's modulus result in high stresses and a lower density and a lower Young's modulus in low stresses. Some boundary effects are visible at the northern and southern model edge, where the compressional boundary conditions are defined, showing the highest values for S_{hmin} and S_{Hmax}. An exception is the stiff Tauern window (Young's modulus: 70 GPa), showing lower magnitudes of S_{hmin} and S_{Hmax} up to 1500 m TVD than the weaker surrounding thrusted units of the Alps (Young's modulus: 23 GPa) do. This is probably due to the fact, that the Tauern window is pushed into the softer units and the soft units absorb the stress. This is also indicated by the high RSR values within the surrounding units (Fig. 11, 500 to 2500 m TVD), indicating high horizontal stresses. Furthermore, remarkable low magnitudes of S_{hmin} and S_{Hmax} occur at the boundary between the RHZ and the MGCH up to 2500 m TVD. This might be an effect due to the vertical boundary between these units (Ahlers et al. 2021a).

The prediction of the stress regime and possible stress regime changes are important for the stimulation of geothermal reservoirs (Azzola et al. 2019), borehole stability and for directional drilling (Rajabi et al. 2016). In particular, if the stress regime change leads to an increase of the differential stress, e.g., due to a change from a normal faulting to a strike-slip faulting regime. For this, the RSR indicating lateral and vertical stress regime changes is a useful parameter. For example, the RSR values in the Glückstadt Graben up to 2500 m TVD, which are higher as in the adjacent areas of the NGB. Probably, the predicted strike-slip regime is related to major salt walls within this region (Maystrenko et al., 2005). The low density of salt (2100 kg/m^3) leads to a relative low S_V magnitude and, as a result, the horizontal stresses exceed S_V and even a thrust faulting regime at 1500 m TVD is partially established. Very low RSR values at 2500 m TVD in the SNB show an opposite effect. The weak Rotliegend sediments with a Young's modulus of 15 GPa lead to low horizontal stresses, and therefore, the RSR value decreases, leading to a normal faulting regime. This is also well visible in the depth section at 5000 m TVD in the NGB. The trend towards relatively higher values in the URG than in the surrounding areas at 5 km TVD is related to a lower S_V in comparison to the graben shoulders because of the sedimentary fill of the URG but similar horizontal stresses. Above 5 km TVD, the horizontal stresses are lower in the URG due to the lower Young's modulus of the sediments. However, at 5 km TVD the basement of the URG is reached with a similar Young's modulus as for

the graben shoulders. In general, a trend towards a normal faulting stress regime due to increasing dominance of S_V with depth is visible. Thus, the depth section at 5000 m TVD shows mainly RSR values smaller than 1.0.

This trend is also clearly visible in Fig. 12. All results displayed show a stress regime change from a dominant strike-slip regime in the uppermost part of the model to a normal faulting regime at 8000 m TVD. However, within the depth range of 200 to 8000 m TVD the results of the individual virtual wells differ sometimes significantly. The results from the NGB show an almost continuous change from a strike-slip regime in the upper 500 m to a normal faulting regime at TVDs > 3000 m with a transition zone between 500 and 3000 m TVD, where the stress regime is not the same for all virtual wells. The virtual wells located in the URG show a more complex stress regime change with depth, with differences up to 7500 m TVD. In the upper 1500 m, the magnitudes of S_V and S_{Hmax} are almost equal resulting in a strike-slip to reverse faulting regime or transpressional regime, respectively. Between 1500 and 2500 m TVD almost all S_{Hmax} magnitudes get higher than S_V resulting in a strike-slip regime. Between ~ 5500 and 7500 m TVD, the stress regime changes to a normal faulting regime. An exception are the results at Bruchsal, showing several changes of the stress regime up to 5500 m TVD between strike-slip and normal faulting regimes. The results of the MB show almost similar results as the results from the URG. Starting with a strike-slip to reverse faulting regime within the upper parts of the model, followed by a strike-slip regime and finally a normal faulting regime.

Conclusions

The model presented is a further step towards a robust prediction of the crustal stress state of Germany with focus on sedimentary basins. It is based on Ahlers et al. (2021a), but significantly improved. An 18-time higher mesh resolution resulting in a lateral resolution of 2.5 km and a vertical resolution of up to 240 m, 15 additional units within the sedimentary layer and an additional model calibration with S_{Hmax} magnitudes, provide a refined prediction of the crustal stress field of Germany. The 3D geomechanical–numerical model provides the complete 3D stress tensor for the entire model volume. Overall, the results show a good fit to all three principal stress magnitudes S_V, S_{hmin} and S_{Hmax} indicated by absolute differences of 0.0 MPa for S_V, 4.6 MPa for S_{hmin} and 6.4 MPa for S_{Hmax}. The differences to the calibration data are mainly within in a range of ± 10 MPa for the S_{hmin} magnitudes and within a range of ± 20 MPa for the S_{Hmax} magnitudes. Despite the overall good fit, some data indicate too low S_{hmin} values in the upper 1500 m TVD of our model. However, additional data from the NGB does not confirm a general trend. Apart from the magnitudes we compare our results also with a mean orientation of S_{Hmax} derived from the WSM (Heidbach et al. 2016) and additional data of Levi et al. (2019). Our predicted orientations of S_{Hmax} show an overall good fit with a median of 0.3° and our results lie almost entirely within the standard deviation of the derived WSM data. However, our model does not resolve perturbations of S_{Hmax} on smaller local scales as indicated by the data of the WSM.

Some limitations result from the size of our model. Due to the size, it is not possible to define visco-elastic properties, e.g., for the Zechstein salt unit. Furthermore, the vertical resolution is still too low to numerically represent all units sufficiently

and at the same time some inhomogeneous units such as the Triassic are still combined. Accordingly, sub modeling is a useful method to enable a higher resolution and stratigraphic refinement (e.g., Ziegler et al. 2016). Such smaller models on local or reservoir scale also enable consideration of varying rock properties (e.g., Ziegler 2021), a quantification of model uncertainties and the implementation of structures that influence the stress field on a local scale, e.g., faults. In addition, more high quality data records, especially magnitude data from north Germany are necessary for a more reliable calibration.

Abbreviations

3DD	3D Deutschland
ALCAPA	Alps–Carpathian–Pannonian
ATA	Armorican Terrane Assemblage
BF	Black Forest
CG	Central Graben
EEC	East European Craton
EI	Eifel
FP	Fracture Potential
HG	Horn Graben
HZ	Harz Mountains
GG	Glückstadt Graben
LRG	Lower Rhine Graben
M	Massif
MDZ	Moldanubian Zone
MGCH	Mid German Crystalline High
OD	Odenwald
OG	Ohře Graben
RHZ	Rhenoherzynian Zone
RSR	Regime Stress Ratio
S_{Hmax}	Maximum horizontal stress
S_{hmin}	Minimum horizontal stress
SNB	Saar–Nahe Basin
SP	Spessart
S_V	Vertical stress
SXZ	Saxothuringian Zone
TVD	True vertical depth
TW	Tauern Window
URG	Upper Rhine Graben
VB	Vogelsberg Complex
VG	Vosges
WSM	World Stress Map

Acknowledgements

This study is part of the SpannEnD Project (http://www.SpannEnD-Projekt.de, last access: 2022/06/17), which is supported by Federal Ministry for Economic Affairs and Energy (BMWI) and managed by Projektträger Karlsruhe (PTKA) (project code: 02E11637A). Calculations for this research were conducted on the Lichtenberg high performance computer of the Technische Universität Darmstadt. Coastlines and borders used in the figures are based on the Global Self-consistent Hierarchical High-resolution Geography (GSHHG) of Wessel and Smith (1996). We acknowledge support by the Deutsche Forschungsgemeinschaft (DFG—German Research Foundation) and the Open Access Publishing Fund of Technische Universität Darmstadt.

Author contributions

Conceptualization of the project was done by AH, TH, KR, OH and BM. Construction, discretization and calibration of the model were done by SA. Data for the model and its calibration were collected and provided by SA, LR, SM, MSW and DA. Evaluation of the model results and their interpretation were performed by SA with the support of AH, TH, KR, BM, LR, OH and SM. SA wrote the paper with help from all coauthors. All authors read and approved the final manuscript.

Funding

Open Access funding enabled and organized by Projekt DEAL. This research has been supported by the Bundesministerium für Wirtschaft und Energie (Grant No. 02E11637A).

Availability of data and materials

The model geometry and the results of our model have been published and are publicly available at: https://doi.org/10.48328/tudatalib-437.5 (see Ahlers et al. 2022).

Declarations

Competing interests

The authors declare that they have no competing interests.

Author details

[1]Engineering Geology, Institute of Applied Geosciences, TU Darmstadt, 64287 Darmstadt, Germany. [2]Technical Petrophysics, Institute of Applied Geosciences, KIT, 76131 Karlsruhe, Germany. [3]Seismic Hazard and Risk Dynamics, GFZ German Research Centre for Geosciences, 14473 Potsdam, Germany. [4]Institute for Applied Geosciences, TU Berlin, 10587 Berlin, Germany. [5]Basin Modelling, GFZ German Research Centre for Geosciences, 14473 Potsdam, Germany. [6]Department of Geology, Geochemistry of Petroleum and Coal, Faculty of Georesources and Material Engineering, RWTH Aachen University, Aachen, Germany.

Received: 1 December 2021 Accepted: 10 June 2022
Published online: 25 June 2022

References

Ahlers S, Hergert T, Henk A. Numerical modelling of salt-related stress decoupling in sedimentary basins-motivated by observational data from the North German Basin. Geosciences. 2019. https://doi.org/10.3390/geosciences9010019.

Ahlers S, Henk A, Hergert T, Reiter K, Müller B, Röckel L, Heidbach O, Morawietz S, Scheck-Wenderoth M, Anikiev D. 3D crustal stress state of Germany according to a data-calibrated geomechanical model. Solid Earth. 2021a;12:1777–99. https://doi.org/10.5194/se-12-1777-2021.

Ahlers S, Henk A, Hergert T, Reiter K, Müller B, Röckel L, Heidbach O, Morawietz S, Scheck-Wenderoth M, and Anikiev D (2022) The Crustal stress state of Germany—results of a 3D geomechnical model v2. TUdatalib. https://doi.org/10.48328/tudatalib-437.5 .

Aichholzer C, Duringer P, Orciani S, Genter A. New stratigraphic interpretation of the Soultz-sous-Forêts 30-year-old geothermal wells calibrated on the recent one from Rittershoffen (Upper Rhine Graben, France). Geothermal Energy. 2016;4:1–26. https://doi.org/10.1186/s40517-016-0055-7.

Alber M, Solibida C. Geomechanical characterization of a host rock for enhanced geothermal system in the North-German Basin. Procedia Engineering. 2017;191:158–63. https://doi.org/10.1016/j.proeng.2017.05.167.

Alber M, Backers T, Bartmann K, Brenne S, Dinter S, Dresen G, Gipper P, Grühser C, Heft S, Meier T, Molenda M, Röske F, Stöckhert F. Abschlussbericht zum Verbundprojekt: Erforschung der Mechanismen und Simulation hydraulisch induzierter Risse in geklüfteten Gesteinen für die Optimierung des Aufschlusses geothermischer Lagerstätten, Ruhr-Universität Bochum, geomecon GmbH, 2015.

Anderson EM. The dynamics of faulting. Trans Edinb Geol Soc. 1905;8:387–402. https://doi.org/10.1144/transed.8.3.387.

Angelier J. Determination of the mean principal directions of stresses for a given fault population. Tectonophysics. 1979;56:T17–26. https://doi.org/10.1016/0040-1951(79)90081-7.

Anikiev D, Lechel A, Gomez Dacal ML, Bott J, Cacace M, Scheck-Wenderoth M. A three-dimensional lithospheric-scale thermal model of Germany. Adv Geosci. 2019;49:225–34. https://doi.org/10.5194/adgeo-49-225-2019.

Asch K. The 1:5 Million International Geological Map of Europe and Adjacent Areas (IGME5000). Hannover: Bundesanstalt für Geowissenschaften und Rohstoffe; 2005.

Azzola J, Valley B, Schmittbuhl J, Genter A. Stress characterization and temporal evolution of borehole failure at the Rittershoffen geothermal project. Solid Earth. 2019;10:1155–80. https://doi.org/10.5194/se-10-1155-2019.

Backers T, Meier T, Gipper P, Munsch P, Bücken D, Nokar K, Dinter S, Grühser C, Heft S, Röske F. Abschlussbericht zum Teilprojekt B: Struktur- und Spannungsfeld im Verbundprojekt MAFA: Parametrisierung von Fazies, Diagenese, Struktur- und Spannungsfeld sowie Optimierung der Testabläufe im Malm zur Verringerung des Erfolgsrisikos, geomecon GmbH, 44 pp., 2017.

Bär K, Reinsch T, Bott J. The PetroPhysical Property Database (P^3)—a global compilation of lab-measured rock properties. Earth Syst Sci Data. 2020;12:2485–515. https://doi.org/10.5194/essd-12-2485-2020.

Brückl E, Behm M, Decker K, Grad M, Guterch A, Keller GR, Thybo H. Crustal structure and active tectonics in the Eastern Alps. Tectonics. 2010. https://doi.org/10.1029/2009TC002491.

Buchmann TJ, Connolly PT. Contemporary kinematics of the Upper Rhine Graben: A 3D finite element approach. Global Planet Change. 2007;58:287–309. https://doi.org/10.1016/j.gloplacha.2007.02.012.

Budach I, Moeck I, Lüschen E, Wolfgramm M. Temporal evolution of fault systems in the Upper Jurassic of the Central German Molasse Basin: case study Unterhaching. Geol Rundsch. 2017;107:635–53. https://doi.org/10.1007/s00531-017-1518-1.

Cacace M, Bayer U, Marotta AM. Strain localization due to structural in-homogeneities in the Central European Basin System. Geol Rundsch. 2008;97:899–913. https://doi.org/10.1007/s00531-007-0192-0.

Cacace M. Stress and strain modelling of the Central European Basin System, Ph. D. thesis, Freie Universität Berlin, Berlin, 167 pp., 2008.

Chang CT, Zoback MD. Viscous rheology and state of stress in unconsolidated sands, rock mechanics in petroleum engineering, Trondheim, Norway. 1998;465–473, https://doi.org/10.2118/47401-MS

Connolly P, Cosgrove J. Prediction of static and dynamic fluid pathways within and around dilational jogs. Geol Soc London Spl Publ. 1999;155:105–21. https://doi.org/10.1144/GSL.SP.1999.155.01.09.

Cornet FH, Röckel T. Vertical stress profiles and the significance of "stress decoupling." Tectonophysics. 2012;581:193–205. https://doi.org/10.1016/j.tecto.2012.01.020.

Cornet FH, Burlet D. Stress field determinations in France by hydraulic tests in boreholes. J Geophys Res-Sol Ea. 1992;97:11829–49. https://doi.org/10.1029/90JB02638.

Drews MC, Seithel R, Savvatis A, Kohl T, Stollhofen H. A normal-faulting stress regime in the Bavarian Foreland Molasse Basin? New evidence from detailed analysis of leak-off and formation integrity tests in the greater Munich Area, SE-Germany. Tectonophysics. 2019;755:1–9. https://doi.org/10.1016/j.tecto.2019.02.011.

Dubelaar CW, Nijland TG. Early Cretaceous Obernkirchen and Bentheim Sandstones from Germany used as dimension stone in the Netherlands: geology, physical properties, architectural use and comparative weathering, in: Geomaterials in construction and their sustainability: understanding their role in modern society, edited by: Přikryl, R., Török, Á., Theodoridou, M., Gomez-Heras, M., and Miskovsky, K., 163–181, https://doi.org/10.1144/SP416.13, 2016.

Eckert A, Connolly P. 2D finite element modelling of regional and local fracture networks in the Eastern California shear zone and coso range, California USA, Transactions - Geothermal Resources Council, 28, 643–648, 2004

Feist-Burkhardt S, Götz AE, Szulc J, Borkhataria R, Geluk M, Haas J, Hornung J, Jordan P, Kempf O, Michalik J, Nawrocki J, Reinhardt L, Ricken W, Röhling H-G, Rüffer T, Török Á, and Zühlke R. Triassic, in: The Geology of Central Europe Volume 1: Precambrian and Palaeozoic; Volume 2: Mesozoic and Cenozoic, edited by: McCann, T., The Geological Society of London, 749–821, https://doi.org/10.1144/CEV2P.1, 2008.

Fleckenstein P, Reuschke G, Müller B, and Connolly P. Predicting stress re-orientations associated with major geological structures in sedimentary sequences, DGMK, 593–5, 90 pp., 2004.

Garrard R, Gonus J, Desroches J, and Bailey E. TBO Bülach-1–1: Data Report - Dossier VI Wireline Logging and Microhydraulic Fracturing, nagra, Arbeitsbericht NAB, 20–08, 2021.

GeORG-Projektteam: Geopotentiale des tieferen Untergrundes im Oberrheingraben: Fachlich-Technischer Abschlussbericht des INTERREG-Projekts GeORG, Teil 4, Freiburg i. Br., 104 pp., 2013.

Grünthal G, Stromeyer D. The recent crustal stress field in Central Europe sensu lato and its quantitative modelling. Geol Mijnbouw. 1994;73:173–80.

Häring MO, Schanz U, Ladner F, Dyer BC. Characterisation of the Basel 1 enhanced geothermal system. Geothermics. 2008;37:469–95. https://doi.org/10.1016/j.geothermics.2008.06.002.

Heidbach O, Reinecker J, Tingay M, Müller B, Sperner B, Fuchs K, Wenzel F. Plate boundary forces are not enough: Second- and third-order stress patterns highlighted in the World Stress Map database. Tectonics. 2007. https://doi.org/10.1029/2007TC002133.

Heidbach O, Hergert T, Reiter K, Giger S. NAB 13–88: Local Stress field sensitivity analysis—Case study Nördlich Langen, Wettingen, 50 pp., 2014.

Heidbach O, Ziegler M, Stromeyer D (2020) Manual of the Tecplot 360 Add-on GeoStress v2.0. World stress map technical report, 20–02, pp 62. https://doi.org/10.5880/wsm.2020.001

Heidbach O, Rajabi M, Reiter K, Ziegler M, WSM Team: World Stress Map Database Release 2016 v1.1, GFZ Data Services , https://doi.org/10.5880/WSM.2016.001, 2016.

Hergert T, Heidbach O, Reiter K, Giger SB, Marschall P. Stress field sensitivity analysis in a sedimentary sequence of the Alpine foreland, Northern Switzerland. Solid Earth. 2015;6:533–52. https://doi.org/10.5194/se-6-533-2015.

Hergert T, Heidbach O. Geomechanical model of the Marmara Sea region-II. 3-D contemporary background stress field. Geophys J Int. 2011;185:1090–102. https://doi.org/10.1111/j.1365-246X.2011.04992.x.

Hergert T. Numerical modelling of the absolute stress state in the Marmara region—a contribution to seismic hazard assessment, Dissertation, Universität Karlsruhe, 2009.

Hudson JA, Harrison JP. Rock masses. In: Hudson JA, Harrison JP. Engineering rock mechanics: an introduction to the principles. Amsterdam: Elsevier; 1997, 141–148, https://doi.org/10.1016/B978-008043864-1/50009-4.

Ingebritsen SE, Manning CE. Geological implications of a permeability-depth curve for the continental crust. Geol. 1999;27:1107. https://doi.org/10.1130/0091-7613(1999)027%3C1107:GIOAPD%3E2.3.CO;2.

Jarosiński M, Beekman F, Bada G, Cloetingh S. Redistribution of recent collision push and ridge push in Central Europe: insights from FEM modelling. Geophys J Int. 2006;167:860–80. https://doi.org/10.1111/j.1365-246X.2006.02979.x.

Kaiser A, Reicherter K, Huebscher C, Gajewski D, Marotta AM, Bayer U. Variation of the present-day stress field within the North German Basin; insights from thin shell FE modeling based on residual GPS velocities. Tectonophysics. 2005;397:55–72. https://doi.org/10.1016/j.tecto.2004.10.009.

Klee G, Rummel F. Hydrofrac stress data for the European HDR research project test site Soultz-Sous-Forets. Int J Rock Mech Min. 1993;30:973–6. https://doi.org/10.1016/0148-9062(93)90054-H.

Kley J, Franzke H-J, Jähne F, Krawczyk C, Lohr T, Reicherter K, Scheck-Wenderoth M, Sippel J, Tanner D, van Gent H. Strain and stress. In: Littke R, Bayer U, Gajewski D, Nelskamp S, editors. Dynamics of complex intracontinental basins: The Central European basin system. Berlin: Springer; 2008. p. 97–124. https://doi.org/10.1007/978-3-540-85085-4_3.

Kley J, Voigt T. Late Cretaceous intraplate thrusting in central Europe: effect of Africa-Iberia-Europe convergence, not Alpine collision. Geology. 2008;36:839–42. https://doi.org/10.1130/G24930A.1.

Krawczyk CM, Rabbel W, Willert S, Hese F, Götze H-J, Gajewski D, SPP-Geophysics Group. Crustal structures and properties in the Central European Basin system from geophysical evidence. In: Littke R, Bayer U, Gajewski D, Nelskamp S, editors. Dynamics of complex intracontinental basins: The Central European basin system. Berlin: Springer; 2008. p. 67–95. https://doi.org/10.1007/978-3-540-85085-4_3.

Kroner U, Romer RL, Linnemann U. The Saxo-Thuringian Zone of the Variscan Orogen as part of Pangea. In: Pre-Mesozoic geology of Saxo-Thuringia: From the Cadomian active margin to the Variscan orogen, edited by: Linnemann, U. and Romer, R. L., Schweizerbart, Stuttgart, 3–16, 2010.

Levi N, Habermueller M, Exner U, Piani E, Wiesmayr G, Decker K. The stress field in the frontal part of the Eastern Alps (Austria) from borehole image log data. Tectonophysics. 2019;769: 228175. https://doi.org/10.1016/j.tecto.2019.228175.

Linnemann U, Romer RL. (Eds.): Pre-Mesozoic geology of Saxo-Thuringia: From the Cadomian active margin to the Variscan orogen, Schweizerbart, Stuttgart, 485 pp., 2010.

Litt T, Schmincke H-U, Frechen M, Schluchter C. Quaternary. In: The Geology of Central Europe Volume 1: Precambrian and Palaeozoic; Volume 2: Mesozoic and Cenozoic, edited by: McCann, T., The Geological Society of London, 1287–1340, https://doi.org/10.1144/CEV2P.8, 2008.

Mardia KV. Statistics of directional data probability and mathematical statistics. London: Academic Press; 1972. p. 380.

Marotta AM, Bayer U, Thybo H, Scheck M. Origin of the regional stress in the North German Basin—results from numerical modelling. Tectonophysics. 2002;360:245–64. https://doi.org/10.1016/S0040-1951(02)00358-X.

Maystrenko Y, Bayer U, Scheck-Wenderoth M. The Glueckstadt Graben, a sedimentary record between the North and Baltic Sea in north Central Europe. Tectonophysics. 2005;397:113–26. https://doi.org/10.1016/j.tecto.2004.10.004.
Maystrenko YP, Scheck-Wenderoth M. 3D lithosphere-scale density model of the Central European Basin System and adjacent areas. Tectonophysics. 2013;601:53–77. https://doi.org/10.1016/j.tecto.2013.04.023.
McCann T. The Geology of Central Europe Volume 1: Precambrian and Palaeozoic; Volume 2: Mesozoic and Cenozoic, The Geological Society of London, 1449 pp., 2008.
McCann T, Kiersnowski H, Krainer K, Vozarova A, Peryt TM, Oplustil S, Stollhofen H, Schneider J, Wetzel A, Boulvain F, Dusar M, Torok A, Haas J, Tait J, and Korner F. Permian. In: The Geology of Central Europe Volume 1: Precambrian and Palaeozoic; Volume 2: Mesozoic and Cenozoic, edited by: McCann, T., The Geological Society of London, 531–597, https://doi.org/10.1144/CEV1P.10, 2008.
Meixner J, Schill E, Gaucher E, Kohl T. Inferring the in situ stress regime in deep sediments: an example from the Bruchsal geothermal site. Geotherm Energy. 2014. https://doi.org/10.1186/s40517-014-0007-z.
Morawietz S, Reiter K. Stress Magnitude Database Germany v1.0, GFZ Data Services , https://doi.org/10.5880/wsm.2020.004, 2020.
Morawietz S, Heidbach O, Reiter K, Ziegler M, Rajabi M, Zimmermann G, Müller B, Tingay M. An open-access stress magnitude database for Germany and adjacent regions. Geothermal Energy. 2020. https://doi.org/10.1186/s40517-020-00178-5.
nagra: Sondierbohrung Benken: Technical Report NTB 00–01, nagra, 288 pp., 2001.
Pienkowski G, Schudack ME, Bosak P, Enay R, Feldman-Olszewska A, Golonka J, Gutowski J, Herngreen G, Jordan P, Krobicki M, Lathuiliere B, Leinfelder RR, Michalik J, Monnig E, Noe-Nygaard N, Palfy J, Pint A, Rasser MW, Reisdorf AG, Schmid DU, Schweigert G, Surlyk F, Wetzel A, Wong TE. Jurassic. In: The Geology of Central Europe Volume 1: Precambrian and Palaeozoic; Volume 2: Mesozoic and Cenozoic, edited by: McCann, T., The Geological Society of London, 823–922, https://doi.org/10.1144/CEV2P.2, 2008.
Przybycin AM, Scheck-Wenderoth M, Schneider M. Assessment of the isostatic state and the load distribution of the European Molasse Basin by means of lithospheric scale 3D structural and 3D gravity modelling. Int J Earth Sci. 2015;104:1405–24. https://doi.org/10.1007/s00531-014-1132-4.
Rajabi M, Tingay M, Heidbach O. The present-day state of tectonic stress in the Darling Basin, Australia: Implications for exploration and production. Mar Petrol Geol. 2016;77:776–90. https://doi.org/10.1016/j.marpetgeo.2016.07.021.
Rasser MW, Harzhauser M, Anistratenko OY, Anistratenko VV, Bassi D, Belak M, Berger J-P, Bianchini G, Cicic S, Cosovic, V, Dolakova N, Drobne K, Filipescu S, Gürs K, Hladilova S, Hrvatovic H, Jelen B, Kasinski JR, Kovac M, Kralj P, Marjanac T, Marton E, Mietto P, Moro A, Nagymarosy A, Nebelsick JH, Nehyba S, Ogorelec B, Oszcypko N, Pavelic D, Pavlovec R, Pavsic J, Petrova P, Piwocki M, Poljak M, Pugliese N, Redzepovic R, Rifelj H, Roetzel R, Skaberne D, Sliva L, Standke G, Tunis G, Vass D, Wagreich M, Wesselingh F. Palaeogene and Neogene. In: The Geology of Central Europe Volume 1: Precambrian and Palaeozoic; Volume 2: Mesozoic and Cenozoic, edited by: McCann, T., The Geological Society of London, 1031–1139, https://doi.org/10.1144/CEV2P.5, 2008.
Reicherter K, Froitzheim N, Jarosinski M, Badura J, Franzke H-J, Hansen M, Hubscher C, Müller R, Poprawa P, Reinecker J, Stackebrandt W, Voigt T, Eynatten H von, Zuchiewicz W. Alpine tectonics north of the Alps, in: The Geology of Central Europe Volume 1: Precambrian and Palaeozoic; Volume 2: Mesozoic and Cenozoic, edited by: McCann T. The Geological Society of London, 1233–1285, https://doi.org/10.1144/CEV2P.7, 2008.
Reiter K. Stress rotation—impact and interaction of rock stiffness and faults. Solid Earth. 2021;12:1287–307. https://doi.org/10.5194/se-12-1287-2021.
Reiter K, Heidbach O. 3-D geomechanical–numerical model of the contemporary crustal stress state in the Alberta Basin (Canada). Solid Earth. 2014;5:1123–49. https://doi.org/10.5194/se-5-1123-2014.
Reyer D. Outcrop analogue studies of rocks from the Northwest German Basin for geothermal exploration and exploitation: Fault zone structure, heterogeneous rock properties, and application to reservoir conditions, PhD, 108 pp., 2013.
Röckel T, Lempp C. Der Spannungszustand im Norddeutschen Becken. Erdöl-Erdgas-Kohle. 2003;119:73–80.
Roth F, Fleckenstein P. Stress orientations found in NE Germany differ from the West European trend. Terra Nova. 2001;13:289–96. https://doi.org/10.1046/j.1365-3121.2001.00357.x.
Scheck-Wenderoth M, Krzywiec P, Zuhlke R, Maystrenko Y, Froitzheim N. Permian to Cretaceous tectonics. In: The Geology of Central Europe Volume 1: Precambrian and Palaeozoic; Volume 2: Mesozoic and Cenozoic, edited by: McCann, T., The Geological Society of London, 999–1030, https://doi.org/10.1144/CEV2P.4, 2008.
Scheck-Wenderoth M, Lamarche J. Crustal memory and basin evolution in the Central European Basin System - new insights from a 3D structural model. Tectonophysics. 2005;397:143–65. https://doi.org/10.1016/j.tecto.2004.10.007.
Seithel R, Steiner U, Müller B, Hecht C, Kohl T. Local stress anomaly in the Bavarian Molasse Basin. Geotherm Energy. 2015. https://doi.org/10.1186/s40517-014-0023-z.
Sheorey PR. A theory for In Situ stresses in isotropic and transverseley isotropic rock. Int J Rock Mech Min. 1994;31:23–34. https://doi.org/10.1016/0148-9062(94)92312-4.
Simpson RW. Quantifying Anderson's fault types. J Geophys Res. 1997;102:17909–19. https://doi.org/10.1029/97JB01274.
Sternai P, Sue C, Husson L, Serpelloni E, Becker TW, Willett SD, Faccenna C, Di Giulio A, Spada G, Jolivet L, Valla P, Petit C, Nocquet J-M, Walpersdorf A, Castelltort S. Present-day uplift of the European Alps: evaluating mechanisms and models of their relative contributions. Earth Sci Rev. 2019;190:589–604. https://doi.org/10.1016/j.earscirev.2019.01.005.
Stöckhert F, Brenne S, Molenda M, Bartmann K, Hoenig S, Alber M. Geomechanische Charakterisierung von Vulkaniten und Sedimenten des Rotliegenden im Norddeutschen Becken für die Optimierung des Aufschlusses geothermischer Lagerstätten, 19. Tagung für Ingenieurgeologie mit Forum für junge Ingenieurgeologen, München 2013, 2013.
Stollhofen H, Bachmann G, Barnasch J, Bayer U, Beutler G, Franz M, Kästner M, Legler B, Mutterlose J, Radies D. Basin Fill - Upper Rotliegend to Early Cretaceous basin development, in: Dynamics of complex intracontinental basins: The Central European basin system, edited by: Littke, R., Bayer, U., Gajewski, D., and Nelskamp, S., Springer, Berlin, Heidelberg, 181–210, https://doi.org/10.1007/978-3-540-85085-4_4, 2008.

Stromeyer D, Heidbach O (2017) Tecplot 360 Add-on GeoStress. GFZ Data Services. https://doi.org/10.5880/wsm.2017.001
Stüwe, K.: Geodynamics of the Lithosphere, Springer Berlin Heidelberg, Berlin, Heidelberg, 493 pp., 2007.
Tašárová ZA, Fullea J, Bielik M, Środa P. Lithospheric structure of Central Europe: Puzzle pieces from Pannonian Basin to Trans-European Suture Zone resolved by geophysical-petrological modeling. Tectonics. 2016;35:722–53. https://doi.org/10.1002/2015TC003935.
Turcotte DL, Schubert G. Geodynamics. 3rd ed. Cambridge: Cambridge Univ Press; 2014. p. 623.
Urai JL, Schléder Z, Spiers CK, Kukla PA. Flow and transport properties of salt rocks. In: Littke R, Bayer U, Gajewski D, Nelskamp S, editors. Dynamics of complex intracontinental basins: The Central European basin system. Berlin: Springer; 2008. p. 277–90.
Valley B, Evans KF. Stress State at Soultz-Sous-Forêts to 5 km Depth from wellbore failure and hydraulic observations, in: Thirty-Second Workshop on Geothermal Reservoir Engineering, 22–24 January 2007, 2007.
Voigt S, Wagreich M, Surlyk F, Walaszczyk I, Ulicny D, Cech S, Voigt T, Wiese F, Wilmsen M, Niebuhr B, Reich M, Funk H, Michalik J, Jagt JW, Felder PJ, Schulf AS. Cretaceous, in: The Geology of Central Europe Volume 1: Precambrian and Palaeozoic; Volume 2: Mesozoic and Cenozoic, edited by: McCann, T., The Geological Society of London, 923–997, https://doi.org/10.1144/CEV2P.3, 2008.
von Eynatten H, Kley J, Dunkl I, Hoffmann V-E, Simon A. Late Cretaceous to Paleogene exhumation in central Europe – localized inversion vs large-scale domal uplift. Solid Earth. 2021;12:935–58. https://doi.org/10.5194/se-12-935-2021.
Wenting L, Völkner E, Minkley W, Popp T. Zusammenstellung der Materialparameter für THM-Modellberechnungen - Ergebnisse aus dem Vorhaben KOSINA, BGR, Hannover, 88 pp., 2017.
Zang A, Stephansson O.: Stress Field of the Earth's Crust, Springer Netherlands, Dordrecht, 322 pp., 2010.
Ziegler PA, Dèzes P. Crustal evolution of Western and Central Europe. Geol Soc London Memoirs. 2006;32:43–56. https://doi.org/10.1144/GSL.MEM.2006.032.01.03.
Ziegler MO, Heidbach O, Reinecker J, Przybycin AM, Scheck-Wenderoth M. A multi-stage 3-D stress field modelling approach exemplified in the Bavarian Molasse Basin. Solid Earth. 2016;7:1365–82. https://doi.org/10.5194/se-7-1365-2016.
Ziegler M, Heidbach O (2019a) Manual of the Matlab Script Stress2Grid v1.1. https://doi.org/10.5880/wsm.2019.002
Ziegler M, Heidbach O (2019b) Matlab Script Stress2Grid v1.1, GitHub [code]. https://doi.org/10.5880/wsm.2019.002
Ziegler MO, Ziebarth M, Reiter K et al. (2019) Python Script Apple PY v1.0. GFZ Data Services [code]. https://doi.org/10.5880/wsm.2019.001
Ziegler MO. Python Script HIPSTER v1.3, GFZ Data Services [code], 2021. https://doi.org/10.5880/wsm.2021.001.
Zoback MD. Reservoir Geomechanics. Cambridge: Cambridge University Press; 2007.

Publisher's Note